Supporting Information (SI) Appendix

Redox-coupled proton transfer mechanism in nitrite reductase revealed by femtosecond crystallography

Authors: Yohta Fukuda, Ka Man Tse, Takanori Nakane, Toru Nakatsu, Mamoru Suzuki, Michihiro Sugahara, Shigeyuki Inoue, Tetsuya Masuda, Fumiaki Yumoto, Naohiro Matsugaki, Eriko Nango, Kensuke Tono, Yasumasa Joti, Takashi Kameshima, Changyong Song, Takaki Hatsui, Makina Yabashi, Osamu Nureki, Michael E. P. Murphy, Tsuyoshi Inoue, So Iwata, and Eiichi Mizohata

1. Supplementary Discussion

1.1. Number of observed residues in the SRX and SFX structures. The amino acid sequence of the wild-type *Af*NiR protein we used here is as follows: MATAAEIAALPRQKVELVDPPFVHAHSQVAEGGPKVVEFTMVIEEKKIVIDDAGTEV HAMAFNGTVPGPLMVVHQDDYLELTLINPETNTLMHNIDFHAATGALGGGGLTEINP GEKTILRFKATKPGVFVYHCAPPGMVPWHVVSGMNGAIMVLPREGLHDGKGKALT YDKIYYVGEQDFYVPRDENGKYKKYEAPGDAYEDTVKVMRTLTPTHVVFNGAVGA LTGDKAMTAAVGEKVLIVHSQANRDTRPHLIGGHGDYVWATGKFNTPPDVDQETW FIPGGAAGAAFYTFQQPGIYAYVNHNLIEAFELGAAAHFKVTGEWNDDLMTSVLAPS GTLVPR/GSILEHHHHHH (the slash represents a thrombin cleavage site). The second Ala corresponds to the forth residue in the native *Af*NiR sequence (1); therefore, we refer to this residue as Ala4. The C-terminus of the native *Af*NiR sequence is Thr340 (underlined). Because we cut the C-terminal His tag using thrombin, the resulted C-terminus of our protein is Arg344 (before the slash). Table S10, which describes the observed regions of each structure, shows that more residues tended to be observed at higher resolution. The 1.30 Å resolution SRX NC structure was the only SRX structure showing the electron density of the C-terminal residue (Arg344) in a monomer (molecule B). The 1.60 Å resolution SFX NC structure also showed the clear electron density around the C-terminal region in a monomer (molecule B) (Fig. S19). Although the resolutions of the SRX RT structures were similar to that of the SFX NC structure, they did not show the electron density around the C-terminal region. Even the SRX RS structure, which was determined at the highest resolution in this study, did not. It is known that N- and C- terminal residues are often disordered and thus they are not observed. Probably because molecules in a microcrystal used for SFX were more ordered than molecules in a large crystal used for SRX, we could observe the C-terminal residue even at 1.60 Å resolution. Although C-terminal Arg344 was close to the T1Cu site (~ 10 Å, Fig. S19), it has no physiological functions because the native C-terminus is Thr340 far from the T1Cu site.

1.2. NO_2^- in the SRX NC^{RT} structure. The SRX NC^{RT} data showed clear electron density above T2Cu (Fig. S9) and the best occupancy for modeled NO_2^- was 100% in each monomer (see Complete Materials and Methods). Given that chemical reactions including the photoreduction of Cu and nitrite reduction are significantly faster at RT than at cryogenic temperature, it is expected that NO_2^- in the SRX NC^{RT} structure is rapidly converted to NO and water, because the reduction of NO_2^- occurs even at cryogenic temperature (2) and the our SRX NC structure also indicated NO_2^- reduction *in crystallo*. However, we do not have experimental evidence to abandon the full occupancy NO_2^- model, even if other models (e.g. mixture of substrate and product) can be assigned, too. We therefore assumed that during data

collection (~ 170 sec), new NO_2^- molecules were supplied to T2Cu after original NO_2^- molecules were reduced and the product was subsequently released from the catalytic site. This assumption is consistent with that the NO_2^- binding mode in the SRX NC^{RT} structure was closer to the vertical mode and hence showed a less reduced state than that in the SRX NC structure (Fig. S9, Table S5). Furthermore, the concentration of NO_2^- supplied to the crystal was high enough (60 mM) to replace the product at the catalytic site.

1.3. Dynamics of water molecules in a putative proton channel. Because aligned water molecules have been found in the substrate pocket of CuNiR crystal structures, they are thought to be involved in the formation of a channel for protons required by nitrite reduction (Fig. S1) (3, 4). These water molecules were also observed in the cryogenic structures in this study. Some of them were however disordered in the SRX and SFX structures determined at RT, while another channel connecting the molecular surface and the T2Cu site retained water molecules at RT (Fig. S20). Fukuda & Inoue (5) also reported that some water molecules in the putative proton channel of thermophilic *Gt*NiR are disordered at 320 K, which is a physiological temperature for the bacterium, although more water molecules in the channel are fixed and hence observed at cryogenic temperature. Therefore, this water dynamics in the proton channel at physiological temperatures may be a universal phenomenon in CuNiRs and play an important role in efficient proton supply to the T2Cu site.

2. Complete Materials and Methods

2.1. Expression and purification of CuNiR from *Alcaligenes faecalis* strain S-6 (*Af*NiR). A plasmid pET28-b containing a start codon, an *Af*NiR gene (Ala^4 to Thr^{340}), a thrombin cleavage site sequence ($L^{341}VPR^{344}/G^{345}SILE^{349}$), and a C-terminal 6×His-tag sequence was transformed into *Escherichia coli* BL21(DE3) strain, which were then grown to an optical density at 600 nm of 0.6–0.8. Expression of the protein was induced with 1 mM isopropylthio-β-D-galactoside at 20 °C for 20 h. The cells were isolated by centrifugation and lysed by sonication in basal buffer A (40 mM Tris-HCl, pH 8.0 and 300 mM NaCl) for the SRX RS^{CL} and SFX RS sample or buffer B (40 mM HEPES-NaOH, pH 7.5) for other samples. The lysate was clarified by centrifugation and passed over a HisTrap HP 5 ml nickel affinity column (GE Healthcare, NJ, USA). After thorough washing with the basal buffer supplemented with 20 mM imidazole, the protein was eluted in the basal buffer supplemented with 250 mM imidazole. Thrombin was added to the eluent containing the target protein for the duration of 12 h dialysis against the basal buffer. The solution was passed through an additional nickel affinity column to remove any undigested *Af*NiR. The solution collected in the initial flow-through was collected and dialyzed against the basal buffers containing 50 mM sodium chloride (for the SRX RS^{CL} and SFX RS sample) or ammonium sulfate (for other

samples), and then loaded onto a HiTrap Q 5 ml ion exchange column (GE Healthcare). The protein was eluted by a linear gradient of sodium chloride or ammonium sulfate from 50 to 1000 mM. The peak fractions were collected, desalted, and concentrated. The final concentration of the *Af*NiR sample was estimated to be 50 mg/ml using the absorption coefficient at 280 nm.

2.2. Expression and purification of the T280V and T280S mutants. The reason for choosing T280V mutant over T280A mutant, is because Ala mutant could possibly allow freer rotation of His255, whereas a Val mutant can provide a similar degree of steric environment as the Thr residue. On the other hand, the reason we chose T280S mutant was because it could donate a hydroxyl O atom to His255 like Thr. The plasmid pET28-b containing the wild-type *Af*NiR gene and the 6×His-tag sequence (described above) was mutated by a polymerase chain reaction method. The forward and reverse primers for the T280V mutation were 5'-GTGGATCAGGAAGTATGGTTTATTCCGGGCGGC-3′ and 5′-GCCGCCCGGAATAAACCATACTTCCTGATCCAC-3′, respectively; whereas the forward and reverse primers for the T280S mutation were 5′-GATCAGGAAAGCTGGTTTATTCCGGG-3′ and 5′-CCCGGAATAAACCAGCTTTCCTGATC-3′, respectively (the codons for the mutations are indicated by underlines). The sequences of the mutant plasmids were confirmed by DNA sequencing before transformation into *E. coli* strain BL21 (DE3). The mutant enzymes were overexpressed and purified following the protocol for the wild-type protein, with the use of buffer B (40 mM HEPES-NaOH, pH 7.5) as the major purification buffer. The final concentrations of the samples were estimated to be 50 mg/ml using the absorption coefficient at 280 nm.

2.3. Nitrite reductase activity assay. Nitrite reductase activity was measured at 25 °C as described by Lawton *et al* (6) with several modifications. The solutions for the assay were prepared inside a glove box (oxygen concentration: < 30 ppm). The starting solution in a screw top cuvette (1 cm cell) contained 2.5 mM $NaNO_2$, 0.5 mM methyl viologen, 0.6 mM dithionite, and 20 mM phosphate buffer (pH 6.3). The cuvette was sealed with a threaded lid containing a rubber septum and inverted several times to ensure an even mixed solution. When the background rate became almost zero, wide-type or mutant CuNiR (100 nM) was added into the cuvette with a glass syringe to initiate the reaction such that the final concentration of *Af*NiR was 1 nM. The oxidation of methyl viologen was monitored at 730 nm (ε = 2,143 M cm^{-1}) using a Cray 50 UV-VIS spectrophotometer (Agilent Technologies, CA, USA). The turnover rate was calculated using the slope in the linear initial rate region. The rates of nitrite reduction for wild-type, T280V, and T280S were 6237 ± 801, 1275 ± 144, 1797 ± 23 s^{-1}, respectively. These data represent an average of three (wild-type and T280V) or

two (T280S) replicates. The rate of nitrite reduction by wild-type *Af*NiR which we reported was one order higher than the value reported by MacPherson *et al*. (7). This is probably because MacPherson *et al.* used 100 mM MES-HEPES buffer (pH 7.0) and *Af*NiR shows lower activity at pH 7.0 than at pH 6.3 (8). Furthermore, as an electron donor, they used a blue copper protein, pseudoazurin, which is a much weaker reductant [E_M = 295 mV at pH 6 (8)] than methyl viologen (E_M ~ - 450 mV *versus* NHE). Therefore, a simple comparison between the previous data and our present data is difficult. However, it is obvious that mutant *Af*NiR proteins showed lower activity than the activity of wild-type *Af*NiR in the same condition.

2.4. Crystallization of *Af*NiR. Macrocrystals used for cryogenic synchrotron X-ray diffraction experiments were prepared by the hanging-drop vapor-diffusion method. Crystals were grown at 20 °C with a 1:1 mixture of the purified protein solution (50 mg/ml) and a reservoir solution composed of 100 mM sodium acetate (pH 4.1) and 7% PEG 4000. Crystals appeared in a few days and reached their maximum size of 1.0 × 0.3 × 0.2 mm in a week. Nanoseed solution was prepared by sonicating the macrocrystals with a UD-211 ultrasonicator (Tomy Seiko Co., Tokyo, Japan) in buffer containing 100 mM sodium acetate (pH 4.0) and 10% PEG 4000. The resulting solution was slightly centrifuged and the upper solution was collected and used as seeds. Microcrystals then were prepared by the rotational seeding crystallization technique. In a 15 ml centrifuge tube, 500 µl of the protein solution (50 mg/ml) was mixed with 10 ml of precipitant solution containing 100 mM sodium acetate (pH 4.0) and 12% PEG 4000, and 20 µl of the nanoseed solution was added. The centrifuge tube was placed on the RT-50 rotator (TITEC, Saitama, Japan) at a speed of 30 rpm for 4 days at room temperature (ca. 293 K) to obtain microcrystals with enough size and amount. The microcrystal solution was filtered through a 30 µm CellTrics filter (Chiyoda Sci. Co., Tokyo, Japan). Sizes of the microcrystals were distributed between 10 and 80 µm, as was observed in a digital microscope KH-8700 (Hirox Co., Tokyo, Japan) (Fig. S5a).

2.5. Synchrotron data collection at cryogenic temperature. Cryogenic SRX datasets for SRX RS and SRX NC were collected at beamline BL26B1 (9) at SPring-8 (Hyogo, Japan). For the preparation of *Af*NiR-NO_2^- complex (SRX NC), a crystal was soaked in the reservoir solution to which glycerol was gradually added to the final concentration of 30% (v/v), and then in the same buffer supplemented with 60 mM sodium nitrite (Wako, Japan) for 15 min. The crystals were frozen in liquid nitrogen and stored until diffraction measurement. Diffraction images were collected at 100 K using a Saturn A200 CCD detector (Rigaku, Tokyo, Japan). The circle beam size was 150 and 100 µm in diameter for the RS and NC samples, respectively. The oscillation angle per image was set to 0.5 °. The exposure time per image was set to 3.8 and 2.0 sec for the RS and NC samples, respectively. A total of 360 and

540 diffraction images were collected for the single RS and NC *Af*NiR crystal, respectively. The parameters and statistics are summarized in Table S1 (SRX RS) and S4 (SRX NC).

The cryogenic SRX dataset for SRX RS^{CL} was collected at beamline BL44XU at SPring-8. The crystal was frozen in liquid nitrogen and stored until diffraction measurement. Diffraction images were collected at 100 K using an MX-300 HE CCD detector (Rayonix, IL, USA). The beam size was 100 μm (Height) × 100 μm (Width). The oscillation angle per image was set to 1.0 °. The exposure time per image was set to 1.0 sec. A total of 720 diffraction images were collected. The parameters and statistics are summarized in Table S8.

2.6. Synchrotron data collection at room temperature (RT). The RT SRX datasets for SRX RS^{RT} and SRX NC^{RT} were collected at beamline BL26B2 at SPring-8. For the preparation of *Af*NiR-NO_2^- complex, a crystal was soaked in the reservoir solution supplemented with 60 mM sodium nitrite for 15 min. MicroLoop and MicroRT X-ray capillary (MiTeGen LLC, NY, USA) were used to mount the crystals on the goniometer. Temperature around the mounted crystal was maintained at 293 K with a N_2 gas stream generator. After setting the crystals on the apparatus, diffraction images were collected using an MX-225 CCD detector (Rayonix, IL, USA). The circle beam size was 100 μm in diameter. The oscillation angle per image was set to 1.0 °. The exposure time per image was set to 1.0 sec. A total of 120 and 170 images were collected for SRX RS^{RT} and SRX NC^{RT}, respectively. For each data collection, a single crystal was used and the exposure position was not changed during data collection. The parameters and statistics are summarized in Table S1 (SRX RS^{RT}) and S4 (SRX NC^{RT}).

2.7. Structure determination of the SRX RS and RS^{CL} structures. The datasets were indexed and integrated using *HKL2000*. The phases were determined by the molecular replacement method using *Phaser* with an *Af*NiR trimer (PDB code ID 1SJM) as a search model. Manual model building was performed using *WinCoot* 0.7. The program *Refmac5* from the *CCP4* suite (ver. 6.5.0) was used for structural refinement. For the high resolution SRX RS structure, anisotropic displacement parameters were introduced after water molecules were built in the models. The final models were checked for stereochemical quality using *MolProbity*. The Cu geometries of the SRX RS and SRX RS^{RT} structures are shown in Table S3. The Cu geometries of the SRX RS^{CL} structures are shown in Table S9.

2.8. Structure determination of the SRX RS^{RT} structure. The datasets were indexed and integrated using *HKL2000*. The phases were determined by the molecular replacement method using *Phaser* with an *Af*NiR trimer (PDB code ID 1SJM) as a search model. Manual model building was performed using *WinCoot* 0.7. The program Refmac5 from the *CCP4* suite (ver. 6.5.0) was used for structural refinement. Anisotropic displacement parameters

were introduced only to Cu atoms after water molecules were built in the models. The final model was checked for stereochemical quality using *MolProbity*. The Cu geometries are shown in Table S3.

2.9. Structure determination of the SRX NC structure. The dataset was indexed and integrated using *HKL2000*. The structure was determined by the molecular replacement method using *Phaser* in the *CCP4* suite (ver. 6.5.0) with an *Af*NiR trimer (PDB code ID 1SJM) as a search model. Manual model building was performed using *WinCoot* 0.7. The program *Refmac5* from the *CCP4* suite was used for structural refinement. Anisotropic displacement parameters were introduced after water molecules were built in the models. Electron densities on the T2Cu sites clearly showed that T2Cu is coordinated by nitrite molecules, however, full occupancy nitrite models showed negative peaks around it in the sigma-A-weighted F_o-F_c map. Therefore, we changed the occupancy of nitrite and found that 95 (molecule A) and 50% (molecule B and C) are the best occupancies. Because there remained positive electron density peaks around the O1 atom of nitrite in molecule B and C, we modeled water molecules with 50% occupancy and residual electron densities were no longer observed. The final model was checked for stereochemical quality using *MolProbity*. The Cu geometries of the SRX NC structure are shown in Table S5.

2.10. Structure determination of the SRX NC^{RT} structure. The dataset was indexed and integrated using *HKL2000*. The structure was determined by the molecular replacement method using *Phaser* in the *CCP4* suite (ver. 6.5.0) with an *Af*NiR trimer (PDB code ID 1SJM) as a search model. Manual model building was performed using *WinCoot* 0.7. The program *Refmac5* from the *CCP4* suite was used for structural refinement. Anisotropic displacement parameters were introduced only to Cu atoms after water molecules were built in the models. Electron densities on the T2Cu sites clearly showed that T2Cu is coordinated by nitrite molecules and we could model full occupancy nitrite on each T2Cu site. There were no positive and negative peaks around the nitrite models in the sigma-A-weighted F_o-F_c map at 3.1 σ, although the full occupancy nitrite model is strange because the rates of chemical reactions such as radiation damages, the photoreduction of Cu, nitrite reduction, are significantly higher at RT than at cryogenic temperature. We discuss this phenomenon in supplementary discussion (*vide supra*). The final model was checked for stereochemical quality using *MolProbity*. The Cu geometries of the SRX NC^{RT} structure are shown in Table S5.

2.11. Single-shot XFEL data collection for the SFX RS structure. The microcrystals of aerobically oxidized *Af*NiR were mixed with a grease matrix, Synthetc grease Super Lube (#21030, Synco Chemical Co.), and packed in an injector syringe (nozzle aperture diameter:

160 μm) before data collection, as described previously (10). The injector was installed in a helium ambiance, diffraction chamber enclosure: Diverse Application Platform for Hard X-ray Diffraction in SACLA (DAPHNIS) (11). The flow rate was set to 1.08 μl/min (896 μm/s) and the liquid-stream width was nearly the same as the aperture size. The sample chamber was maintained at a temperature of 293 K with a humidity of 85–99%. The diffraction patterns were collected using a short-working-distance octal multiport CCD detector (12) with XFEL radiation at BL3 (EH4) of SACLA (Hyogo, Japan). The microcrystals were exposed to single X-ray pulses at a photon energy of 7.0 keV. The pulses were of 2–10 fs duration and consisted of 3×10^{10} photons/pulse focused to 2.0 μm (H) × 2.0 μm (W) at the interaction point using Kirkpatrick–Baez mirrors (13). The repetition rate was 30 Hz, and the typical pulse energy at the sample was 32 μJ/pulse. The pulse duration shorter than 10 fs, we used, is necessary to obtain a "damage-free" metalloprotein structure, because ultrabright XFEL beams damage electronic structures of heavy atoms in a few tens of femtoseconds (14) and can destroy the natural structures of metal centers in metalloproteins (15).

2.12. Single-shot XFEL data collection for the SFX NC structure. The XFEL diffraction patterns were collected at the BL3 (EH4) of SACLA as above. To prepare *Af*NiR NC, 1.2 M sodium nitrite in the precipitant solution was added to the microcrystal sample in a 1.5 ml tube to give a final concentration of 60 mM. After incubation for 5 min, the sample was mixed with the grease matrix and packed in an injector syringe before data collection. To avoid the self-dismutation of NO_2^- ($3NO_2^- + 2H^+ \rightarrow 2NO + NO_3^- + H_2O$), which may occur during the long room-temperature measurement common in SFX, the totaled 18 samples of *Af*NiR-NO_2^- microcrystals were prepared at time of use and data collection for each sample was completed within 50 min after addition of sodium nitrite. The crystal-to-detector distance and the flow rate were set to 49 mm and 1.08 μl/min (896 μm/s), respectively. The sample-stream width from the injector was nearly the same as its nozzle aperture diameter: 160 μm. The sample chamber was maintained at 293 K with a humidity of 30–50%. The microcrystals were exposed to single X-ray pulses at a photon energy of 10.8 keV. The pulses were of 2–10 fs duration and consisted of 1.2×10^{11} photons/pulse focused to 1.3 μm (H) × 1.8 μm (W) at the interaction point using Kirkpatrick–Baez mirrors. The repetition rate was 30 Hz, and the typical pulse energy at the sample was 210 μJ/pulse.

2.13. Structure determination of the SFX RS structure. A total of 83,594 diffraction images were collected. With *Cheetah* (16) adapted for SACLA API (17), these images were filtered to reject those with less than 20 spots. 42,265 hit images were then processed with *CrystFEL* (pre-release version of 0.6.0) using a detector geometry optimized by *geoptimiser*. Integration and background mask parameter (--*int-radius* option in *indexamajig*) was "3,4,7".

No saturation cutoff was applied. Detector background was estimated by averaging dark images and subtracted from diffraction patterns. Indexing was performed by *DirAx*. 21,009 images were indexed in space group $P2_12_12_1$ with unit cell parameters a = 63.1, b = 103.8, and c = 147.8 Å. The indexed diffraction images were integrated and merged using *CrystFEL*. The resolution of the SFX RS structure (2.03 Å) was determined by consulting the R_{split} and $CC_{1/2}$ values (Fig. S21a). The phase was determined by the molecular replacement method using *Phaser* with the *Af*NiR trimer (PDB code ID 1SJM) as a search model. Manual model building was carried out using *WinCoot* 0.7. The program *Refmac5* from the *CCP4* suite (ver. 6.5.0) was used for structural refinement. When the structure was refined, the electron density on T2Cu was first assigned to fully occupied water. However, the *B*-factor of the resulting water molecule was unusually smaller than those of other surrounding atoms and positive electron density remained at the position in the sigma-A-weighted F_o–F_c map. Therefore, chloride was assigned because Tris-HCl buffer was used in purification of the SFX RS sample and T2Cu in CuNiR is often bound by chloride (18). This finding made us change purification conditions for the sample of the NC state (see the purification section described above), because chloride may be able to inhibit the binding of nitrite. The final model was checked for stereochemical quality using MolProbity. The parameters and statistics are summarized in Table S4. The Cu geometries are shown in Table S3.

2.14. Structure determination of the SFX NC structure. A total of 578,412 diffraction images were collected. These images were retrieved through SACLA API and filtered by *Cheetah* to reject images with less than 20 spots. Resulting 194,372 images were then processed with *CrystFEL* as described above. 155,588 images were indexed in space group $P2_12_12_1$ with unit cell parameters a = 63.0, b = 103.0, and c = 147.4 Å. The indexed diffraction images were merged using *CrystFEL*. The R_{split} and the $CC_{1/2}$ values were plotted against resolutions in Fig. S21b.

The phase was determined by the SAD method using Cu as a phasing element. The protocol was same as recent S-SAD phasing at SACLA described elsewhere (19). First, intensities merged by *CrystFEL* were converted to XDS_ASCII format (20) and processed by *SHELXC*. Substructure determination was performed by *SHELXD* using reflections up to 2.1 Å. All of the six copper atoms in the asymmetric unit were located. There was a clear drop in the occupancy between the sixth (correct) site and the seventh (false) site. Phase calculation was carried out with *SHELXE* using reflections up to 1.6 Å by iteration of density modification and automatic chain tracing (Fig. S6). 838 residues out of 1026 residues were automatically traced as polyalanines. Compared to S-SAD phasing, this Cu-SAD was easier and insensitive to parameters; the substructure was solved in less than 100 *SHELXD* trials, while S-SAD required more than 320,000 trials. *SHELXE* solved the structure regardless of the solvent content specified to the program (-*s* parameter ranging from 42% to 56 %) when reflections

better than 2.0 Å were used. In contrast, many *SHELXE* runs with different combinations of parameters had to be tested for successful S-SAD phasing. This is possibly due to larger anomalous difference in this Cu-SAD [about 1.65 % according to the formula by Hendrickson & Teeter (21)] than previous S-SAD (1.58 %).

The maximum resolution of the SFX NC structure was determined by consulting the results of "paired refinement" (Fig. S22) based on the idea that proper use of weaker and noisier but higher-resolution data can provide better models (22-24). Inclusion of higher resolution data up to 1.45 Å resolution led to the improvement of the model. However, the overall R_{work} and overall R_{free} values gradually increased with resolution. We here chose to use data up to 1.60 Å resolution, and performed further refinement. $CC_{1/2}$ and the estimated true *CC* (*CC**) in the highest resolution shell cut at 1.60 Å resolution were 0.251 and 0.633, respectively. Manual model building was carried out using *WinCoot* 0.7. The program *Refmac5* from the *CCP4* suite (ver. 6.5.0) was used for structural refinement. Anisotropic displacement parameters were introduced only to Cu atoms after water molecules were built in the models. For comparison, the dataset was also phased by molecular replacement with *Phaser* using *Af*NiR trimer (PDB code ID 1SJM) as a search model. Because the models determined by Cu-SAD and molecular replacement did not show any significant difference, we adopted the former model, as it is free from a model bias. The final model was checked for stereochemical quality using *MolProbity*. The parameters and statistics are summarized in Table S7. The Cu geometries of the SFX NC structure are shown in Table S5.

3. SI Figures

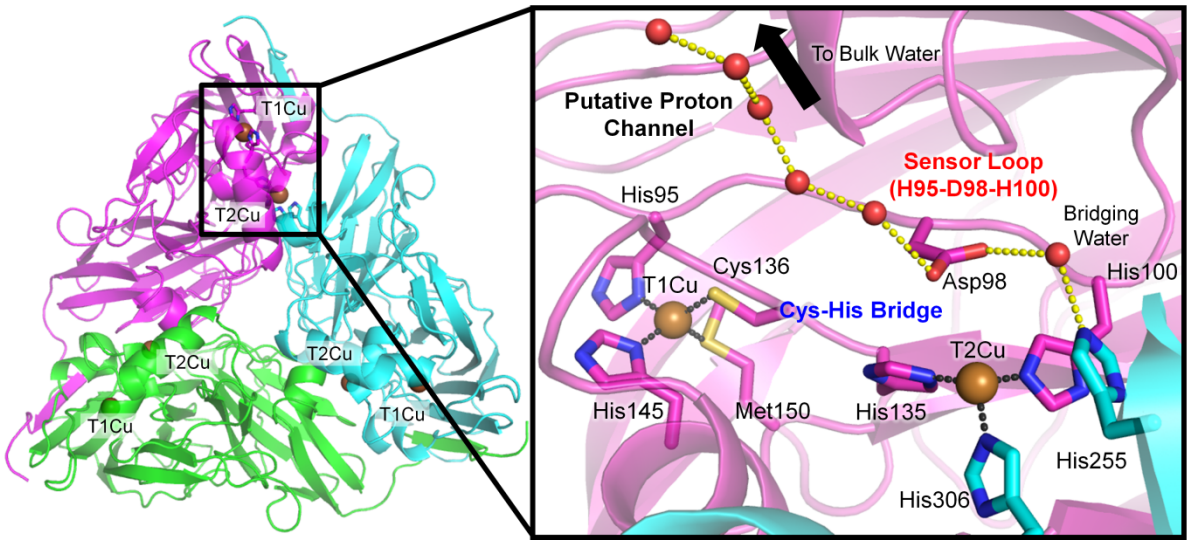

Fig. S1. Structural overview of the two Cu sites in CuNiR (PDB code ID 1AS7) (29). T2Cu is located at the interface between two monomers. Water molecules aligned from the molecular surface to the catalytic site are thought to be a proton channel (3, 4). Each CuNiR monomer was shown by different colors (magenta, cyan, and green). The inset shows a close-up view of the Cu sites. Carbon atoms in one monomer and the other one are colored magenta and cyan, respectively. Nitrogen, oxygen and Cu atoms are colored blue, red and brown. Water molecules and Cu atoms are shown as spheres. Dashed yellow and black lines show hydrogen bonds and coordination bonds, respectively.

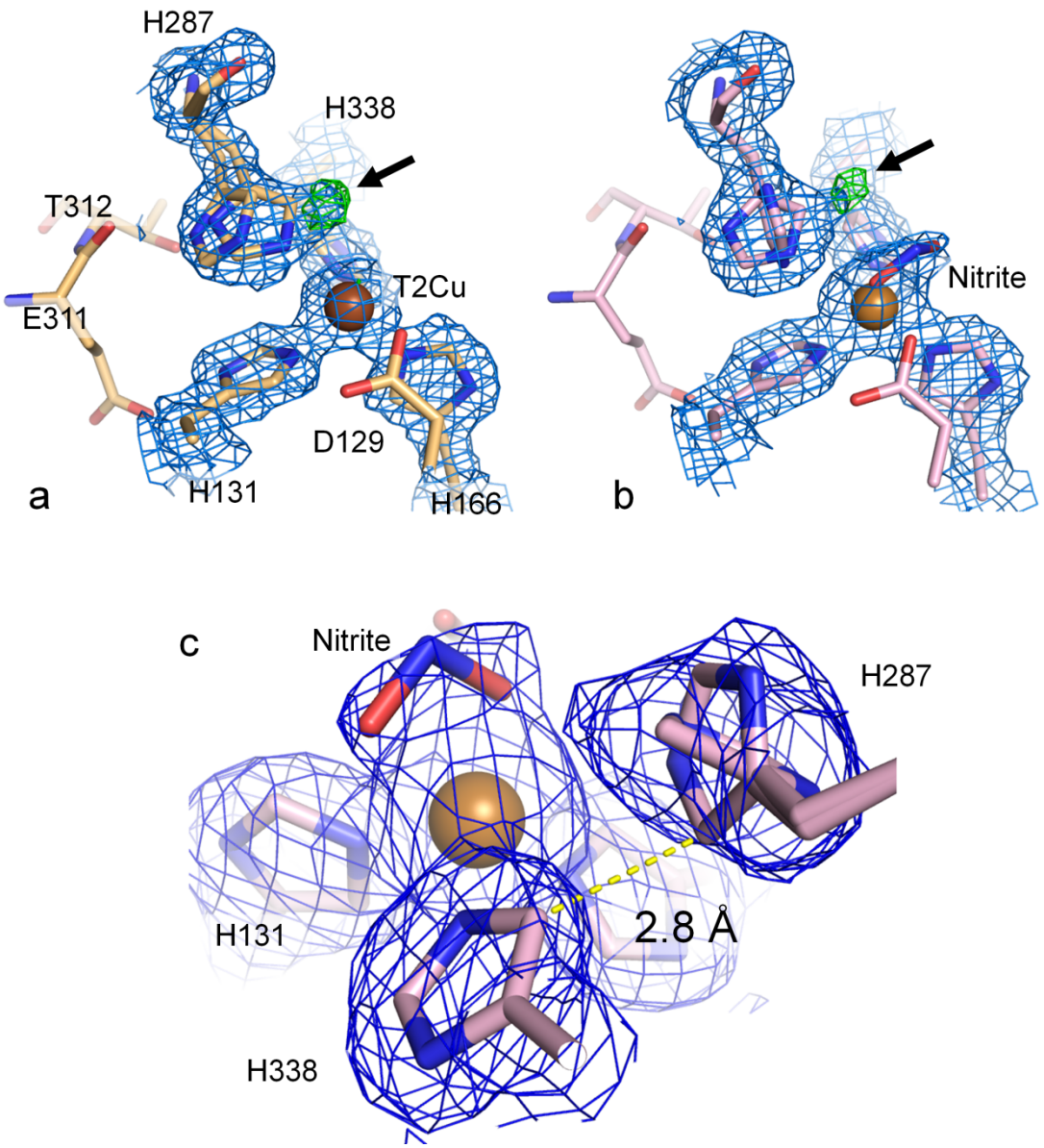

Fig. S2. Unusual electron density (black arrow) around His287 in *Rhs*NiR. The sigma-A-weighted $2F_o–F_c$ map (1.0 σ) and $F_o–F_c$ map (4.0 σ) are shown as blue and green meshes, respectively. (a) The resting state structure determined (1.74 Å resolution, PDB ID: 1ZV2) (30). (b) The nitrite complex structure determined (1.85 Å resolution, PDB ID: 2WDS) (31). (c) Unusually close contact between His287 and His338 in 2WDS. The NO_2^- model does not fit the electron density. We only used the deposited files in PDB and did not refine these structures to draw these figures.

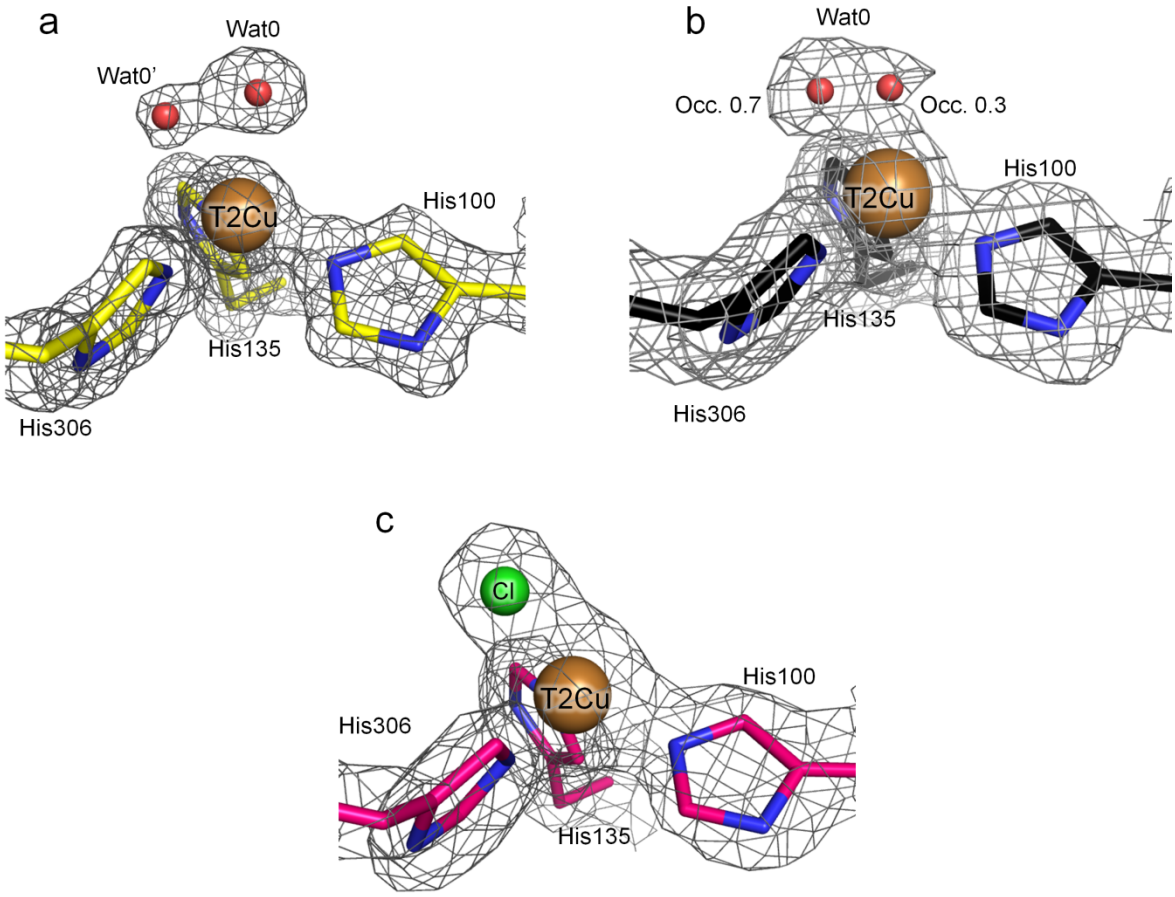

Fig. S3. Comparison between the SRX RS and SFX RS structures. (a) Coordinate structure of the T2Cu site in the SRX RS structure. The sigma-A-weighted $2F_o–F_c$ map (1.5 σ) is shown as gray meshes. (b) Coordinate structure of the T2Cu site in the SRX RS^{RT} structure. The sigma-A-weighted $2F_o–F_c$ map (1.0 σ) is shown as gray meshes. While two different water molecules (Wat 0 and Wat 0´) with full occupancy were modeled on T2Cu in the SRX RS structure, the ligand water molecule on T2Cu in the SRX RS^{RT} structure shows a dual conformation with partial occupancy (70 and 30%). (c) Coordinate structure of the T2Cu site in the SFX RS structure. The sigma-A-weighted $2F_o–F_c$ map (1.5 σ) is shown as gray meshes.

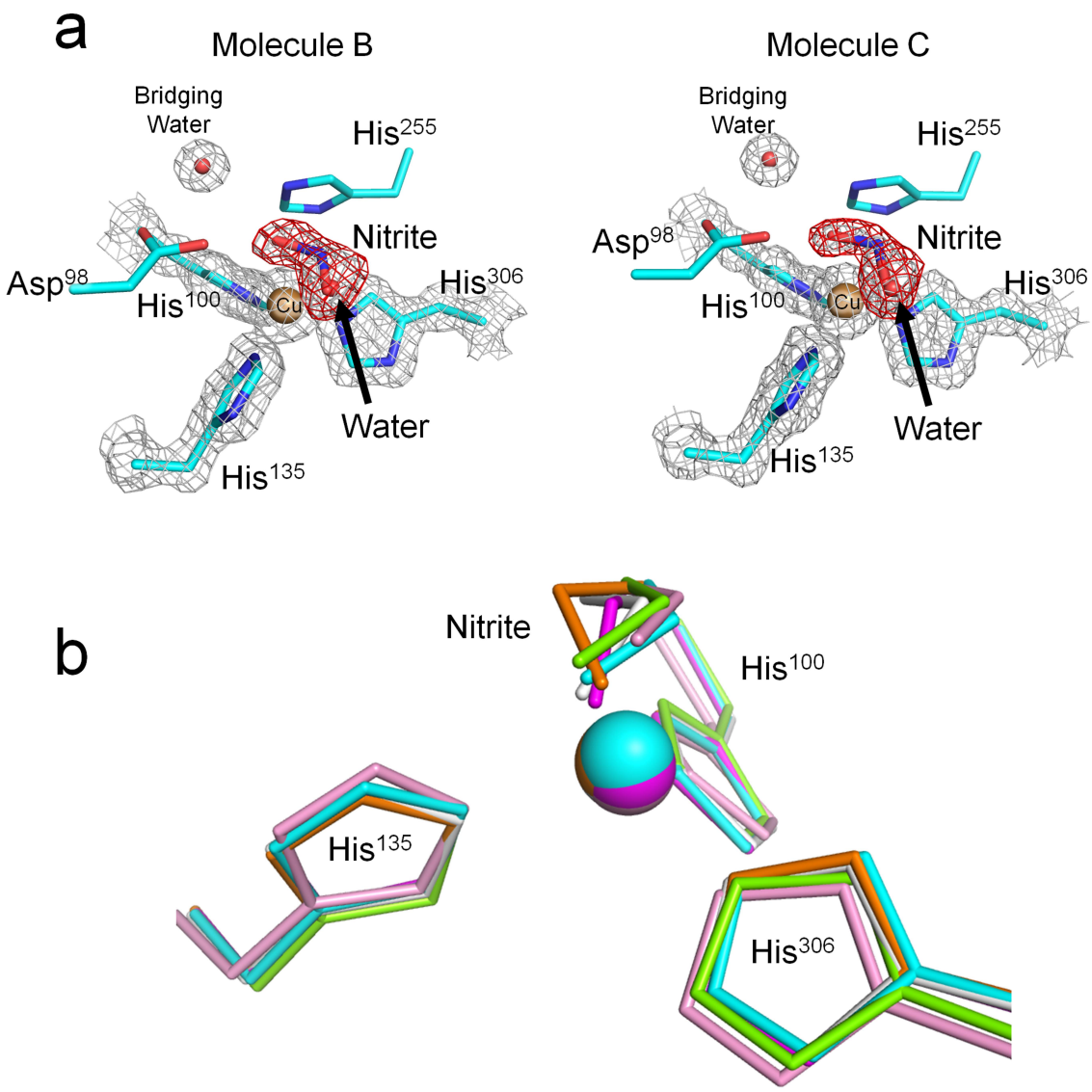

Fig. S4. Nitrite binding in the NC structures. (a) The T2Cu site in the SRX NC structure. The sigma-A-weighted $2F_o–F_c$ (1.5 σ) and omit $F_o–F_c$ (6.5 σ) maps are shown as the gray and red mesh, respectively. Carbon, nitrogen, oxygen and Cu atoms are colored cyan, blue, red and brown. (b) Comparison of directions of nitrite. Cyan: the current SRX NC structure. Magenta: the SFX NC structure. Orange: *Af*NiR (PDB code 1SJM) (27). White: CuNiR from *Achromobacter cycloclastes* (2BWI) (4). Yellow green: CuNiR from *Neisseria gnorrhoeae* (1KBV) (28). Pink: CuNiR from *Geobacillus thermodenitrificans* (3X1N) (5).

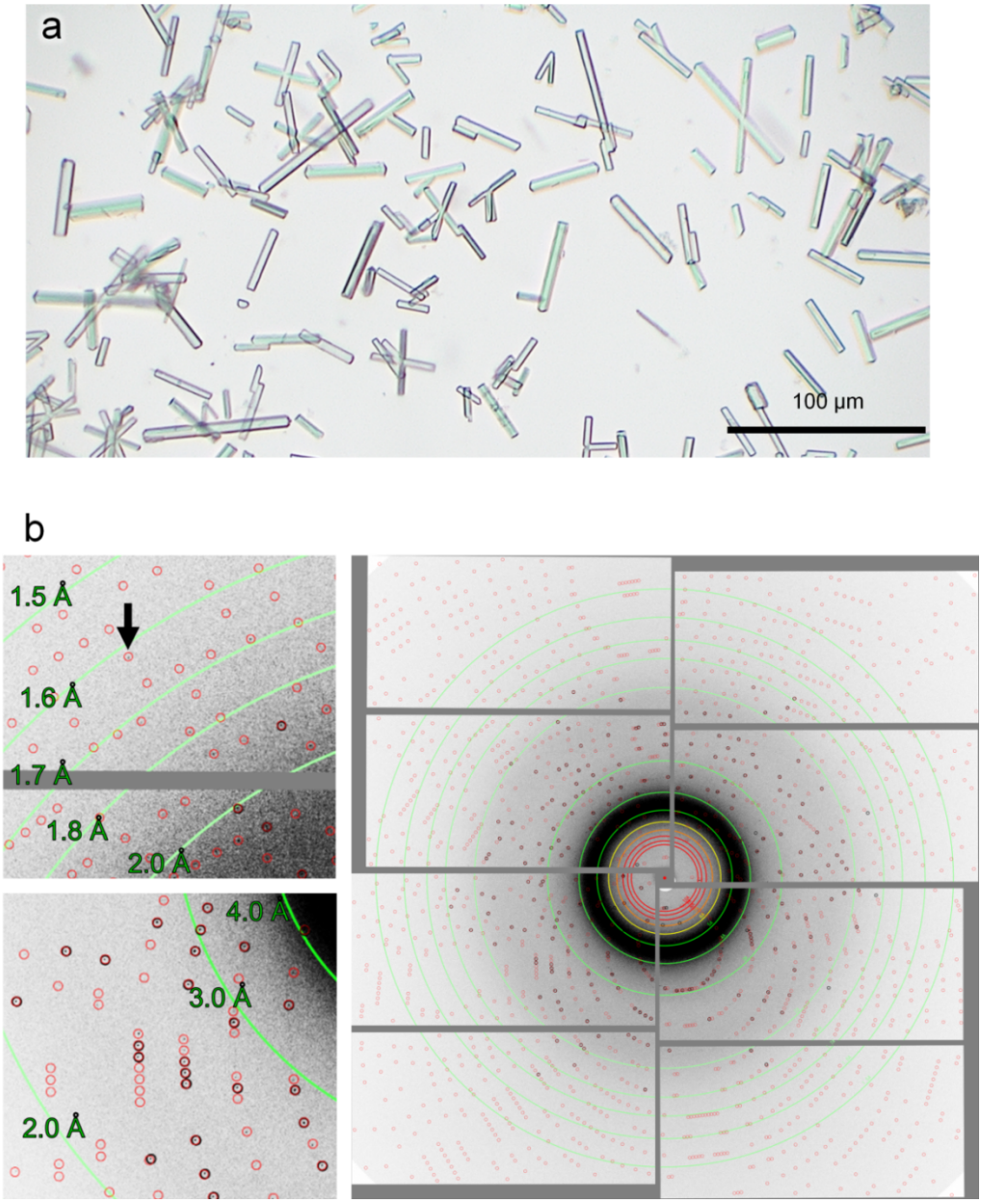

Fig. S5. Serial femtosecond crystallography (SFX). (a) Microcrystals of *Af*NiR. (b) One of the diffraction images from the *Af*NiR NC microcrystals. One of the diffraction spots visible to the naked eye and around 1.6 Å resolution is shown by a black arrow. The spots circled in black were used for indexing, and the red circles show the expected positions of the diffraction spots.

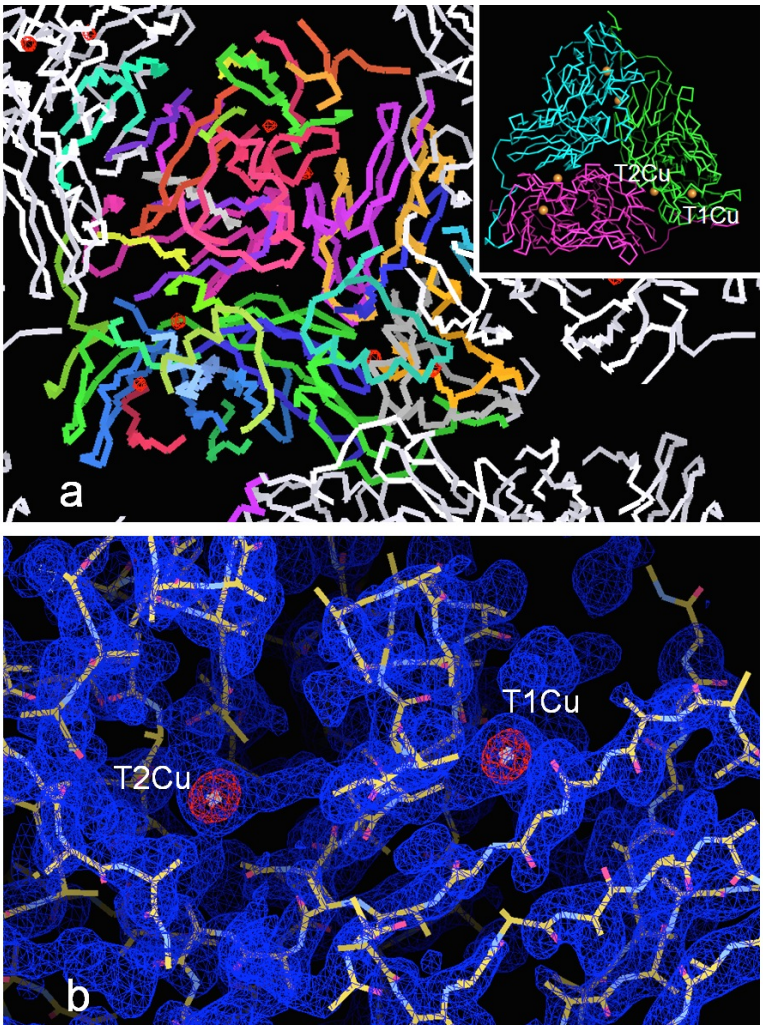

Fig. S6. SAD phasing for the SFX NC data. (a) The anomalous peaks of Cu sites. The anomalous maps are shown by red meshes (contoured at 10 σ). Autotraced poly-alanine chains in an asymmetric unit are colored and molecules generated by symmetric operations are shown by white chains. Inset displays the final refined model. (b) The sigma-A-weighted $2F_o–F_c$ map (blue mesh, contoured at 1.0 σ) after density modification and chain tracing. The anomalous Cu peaks are shown by red meshes (contoured at 10 σ).

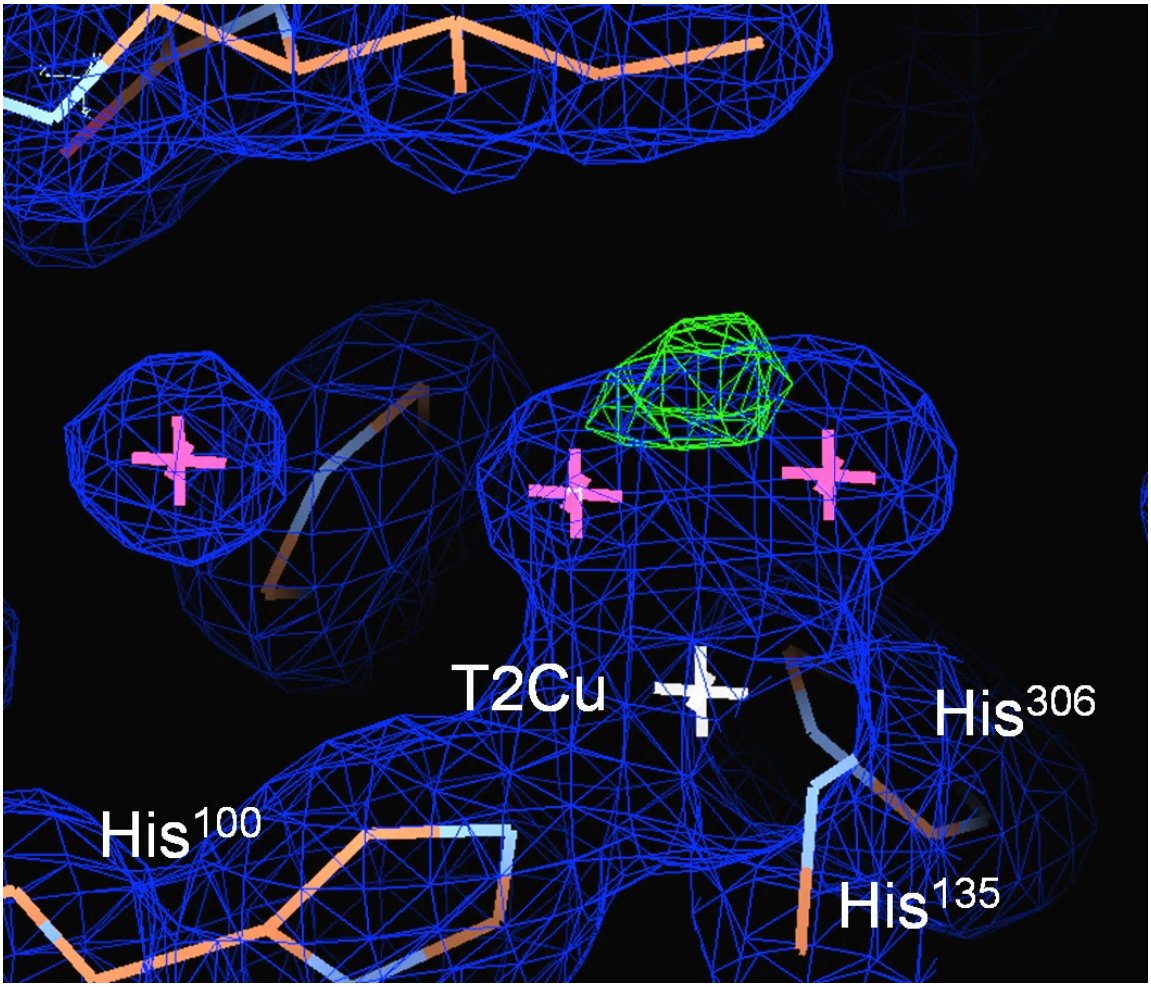

Fig. S7. Electron density above the T2Cu atom in the SFX NC structure in which two water molecules with full occupancy are modeled. The sigma-A-weighted $2F_o–F_c$ map (1.3 σ) is shown as the blue mesh. The positive electron density peak in the sigma-A-weighted $F_o–F_c$ map (4.0 σ) is shown as the green mesh. This figure shows that the electron density above the T2Cu atom should accommodate a bent triatomic molecule.

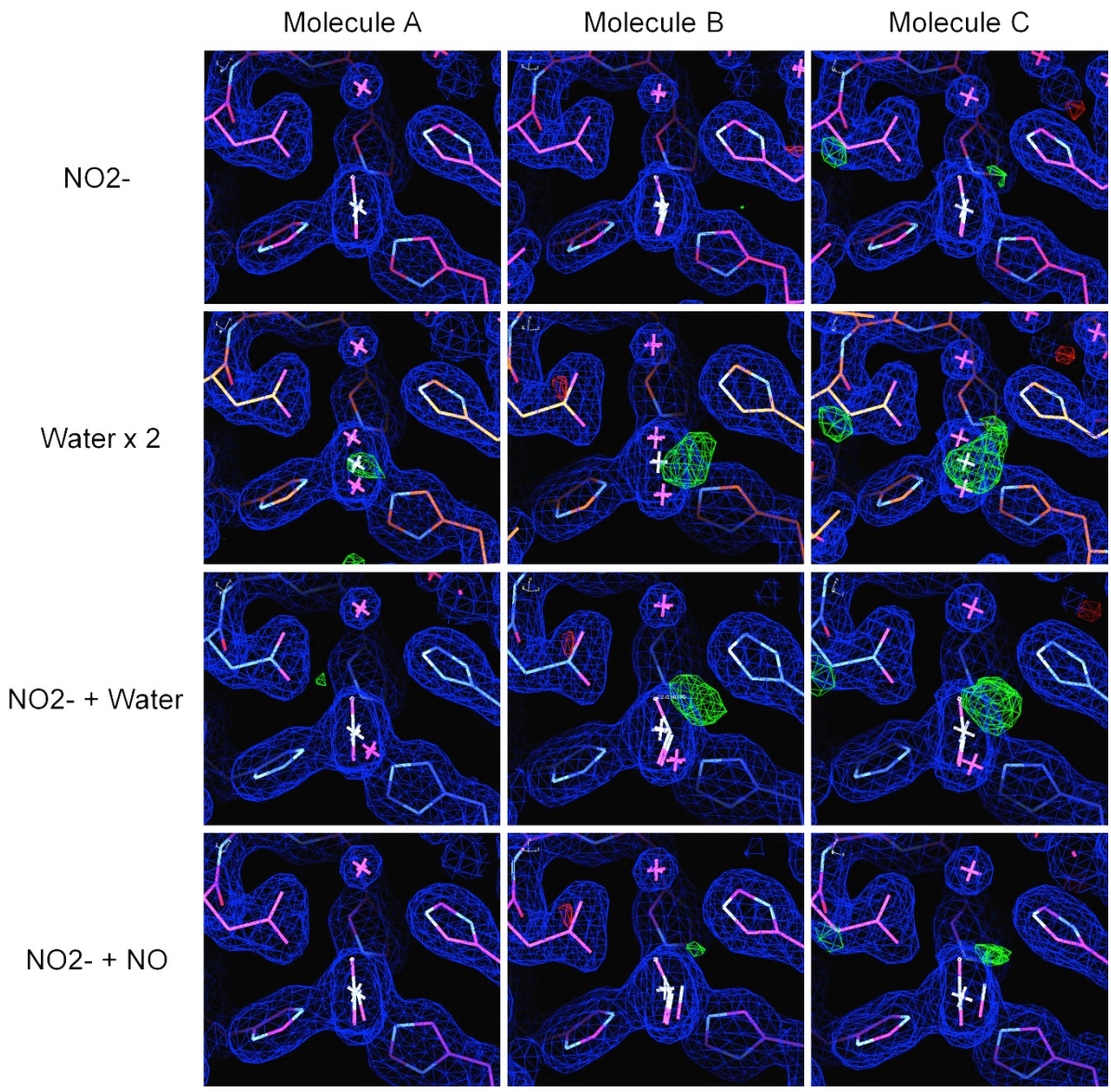

Fig. S8. Residual electron density in several models of the SFX NC structure. The sigma-A-weighted $2F_o–F_c$ (1.3 σ) and $F_o–F_c$ (3.0 σ) positive and negative maps are shown as the blue, green, and red mesh, respectively. When NO_2^- and NO (or water) are modeled at the same time as alternative molecules with 0.5 occupancies, the NO (or water) molecule is deviated from the T2Cu atom.

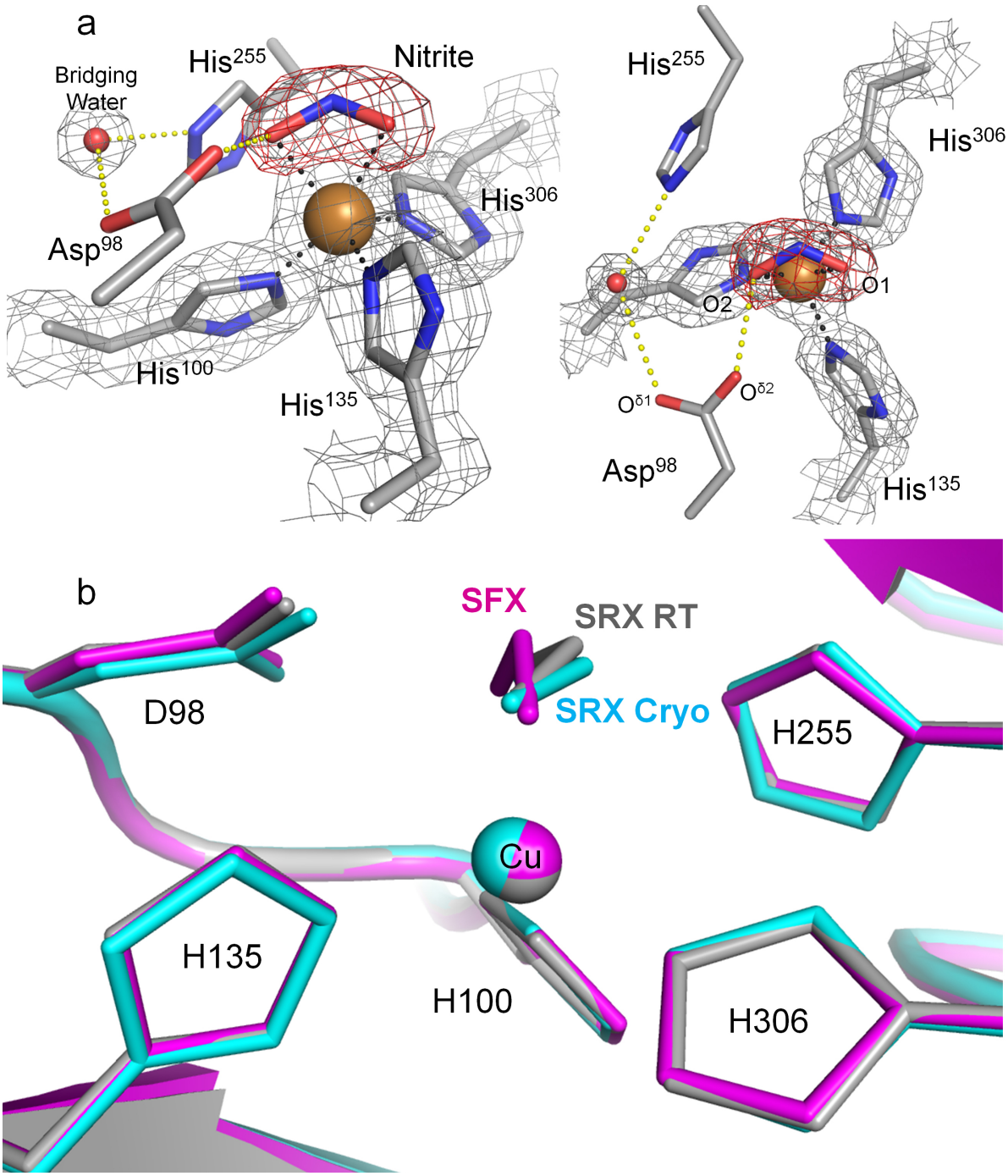

Fig. S9. NO_2^- binding in the SRX NC^{RT} structure. (a) T2Cu site in the SRX NC^{RT} structure (molecule A). The sigma-A-weighted $2F_o–F_c$ (1.5 σ) and omit $F_o–F_c$ (6.5 σ) maps are shown as gray and red meshes, respectively. H-bonds (yellow) and coordination bonds (black) are represented by dashed lines. Carbon, nitrogen, oxygen and Cu atoms are colored gray, blue, red and brown. (b) Comparison between the SFX NC (magenta) , SRX NC (cyan), and SRX NC^{RT} (gray) structures (molecule A).

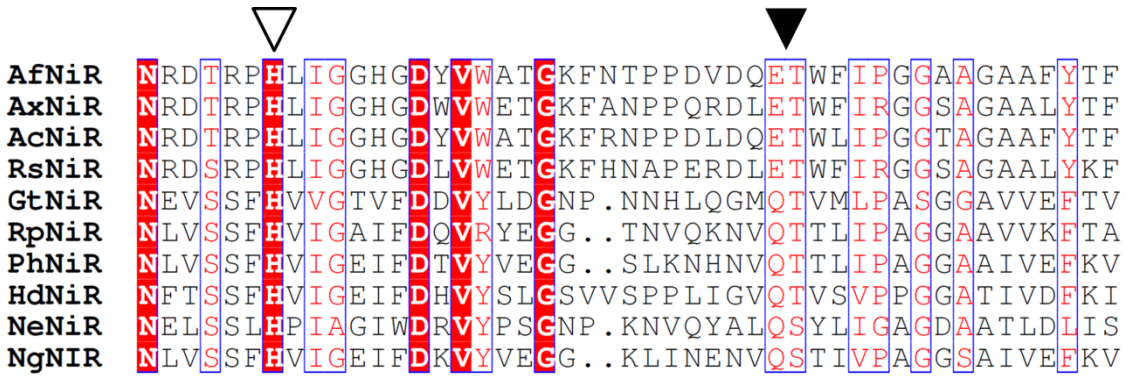

Fig. S10. Amino-acid-sequence alignment of CuNiRs. The position of His255 in *Af*NiR is indicated by an open triangle. The position of the conserved pair of Glu (or Gln) and Thr (or Ser) is indicated by a filled triangle. Ax, Ac, Rs, Gt, Rp, Ph, Hd, Ne, and Ng means *Achromobacter xylosoxidans*, *Achromobacter cycloclastes*, *Rhodobacter sphaeroides*, *Geobacillus thermodenitrificans*, *Ralstonia pickettii*, *Pseudoalteromonas haloplanktis*, *Hyphomicrobium denitrificans*, *Nitrosomonas europaea*, and *Neisseria gonorrhoeae*, respectively. Sequence alignment was performed with ClustalW (25) and the figure was generated by ESPript3 (http://espript.ibcp.fr) (26).

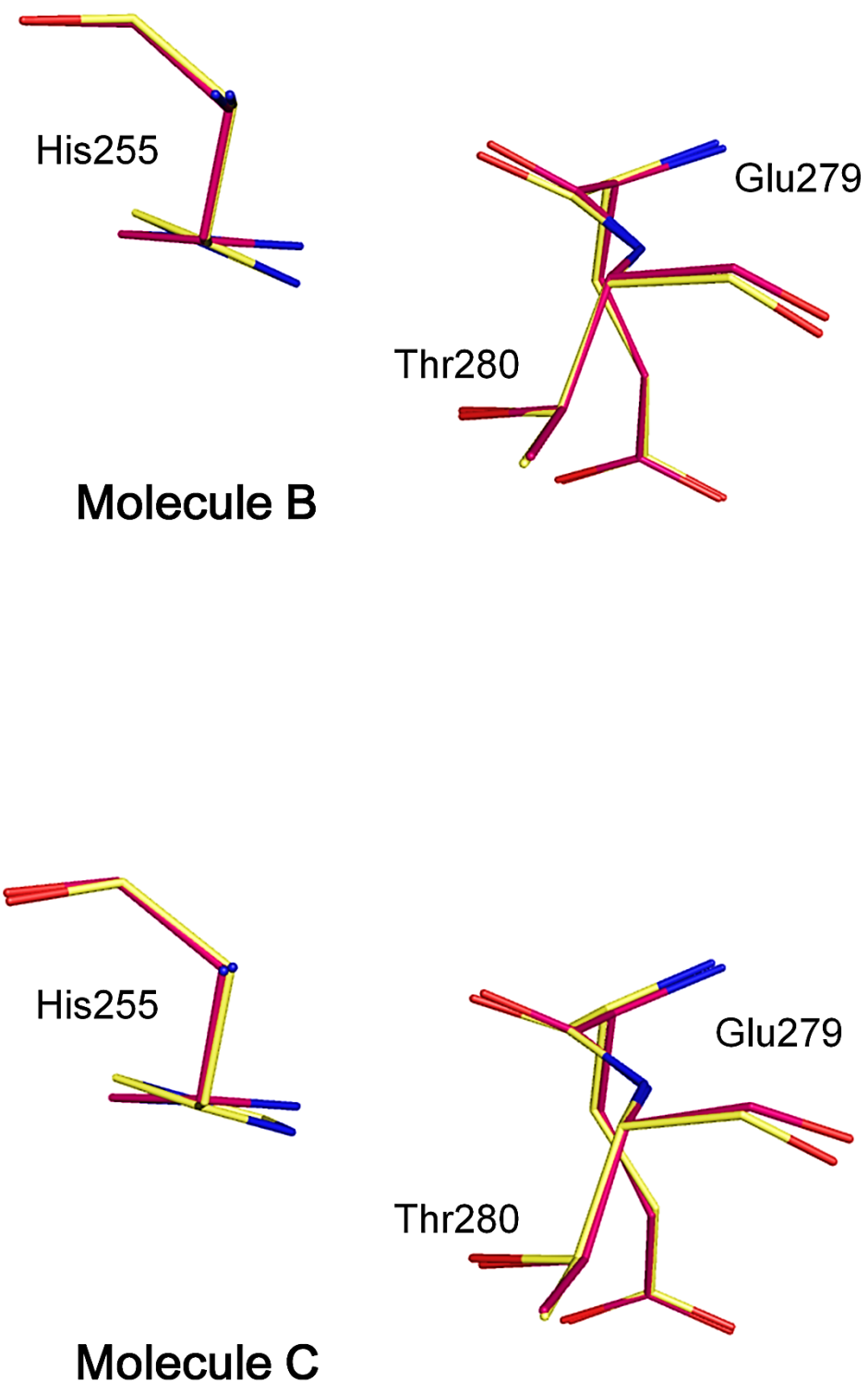

Fig. S11. Structural comparison of His255 in molecules B and C of the SFX RS (hot pink) and SRX RS (yellow) structures.

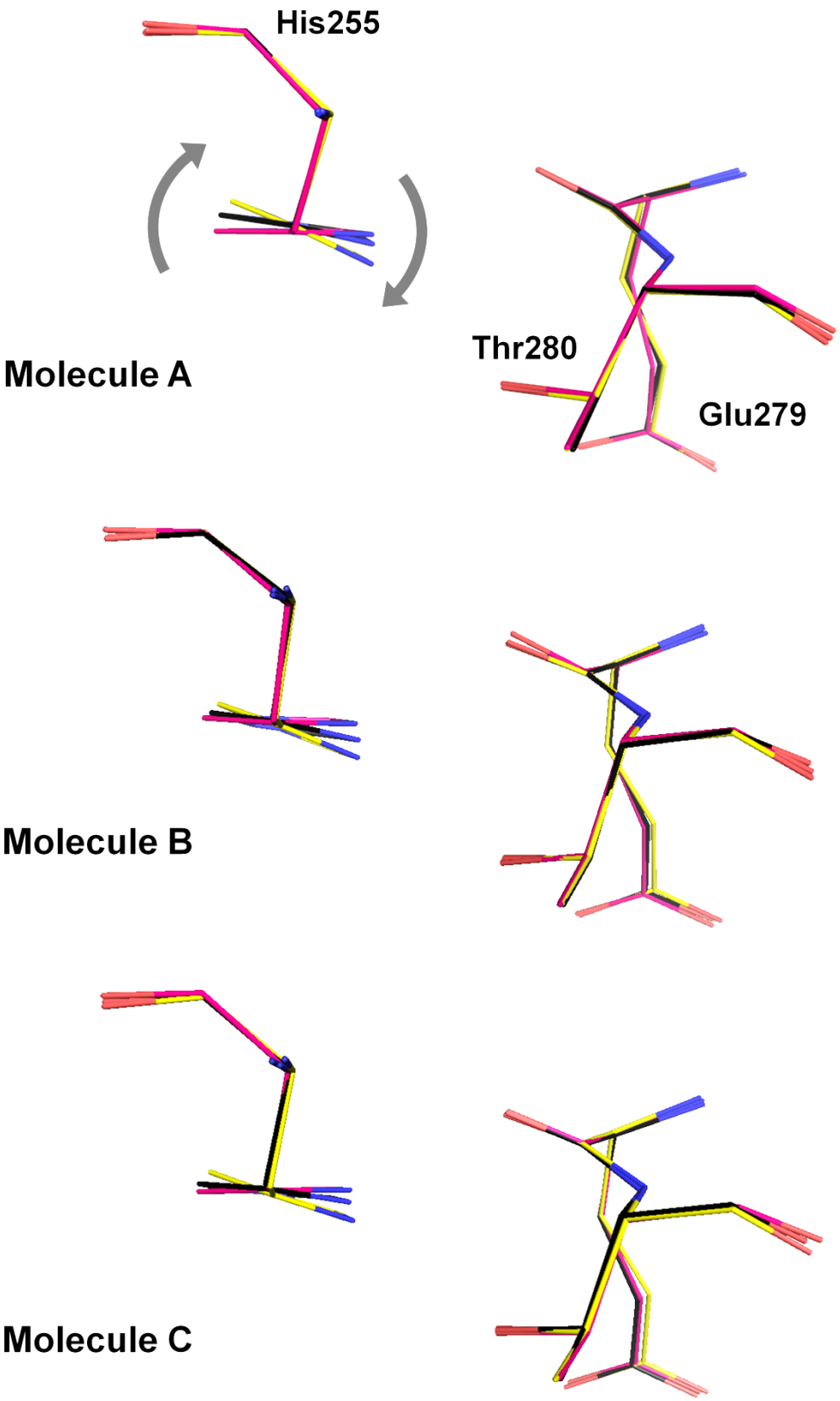

Fig. S12. Structural comparison of His255 of the SFX RS (hot pink), SRX RS (yellow), and SRX RS^{RT} (black) structures.

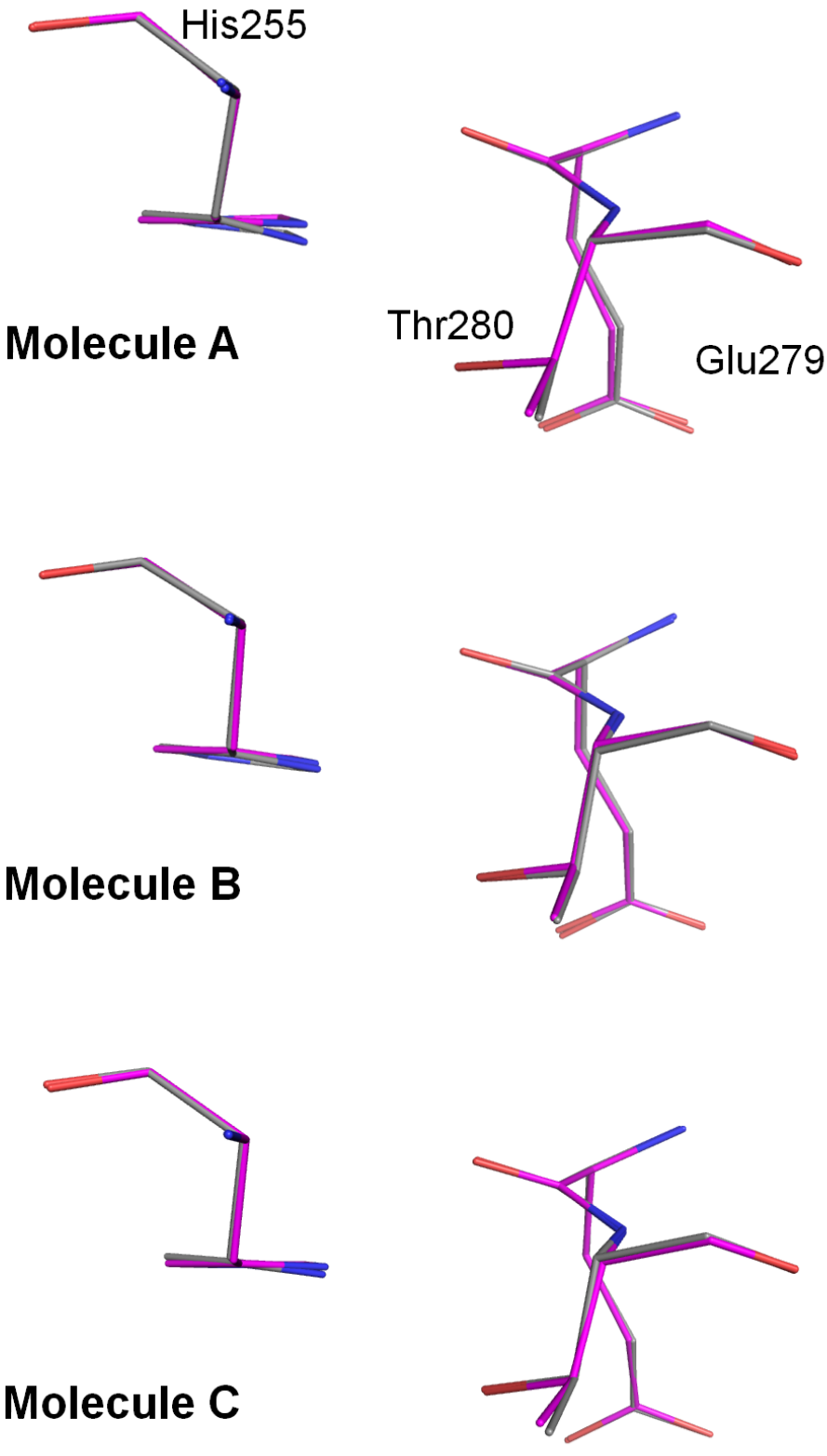

Fig. S13. Structural comparison of His255 of the SFX NC (magenta) and SRX NC^{RT} (gray) structures.

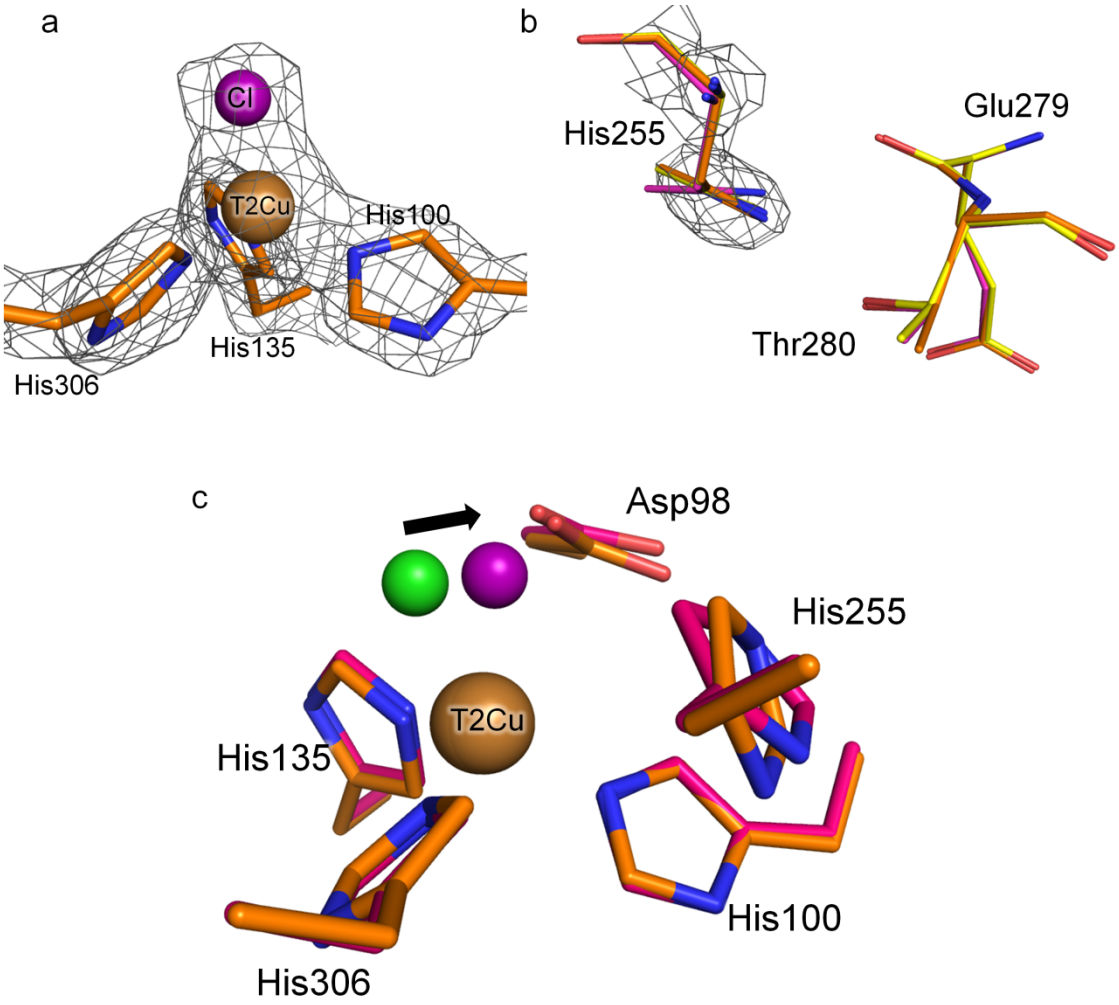

Fig. S14. The T2Cu site in the SRX RS^{CL} structure. (a) Coordinate structure of the T2Cu site. The sigma-A-weighted $2F_o$-F_c map (1.5 σ) is shown as a gray mesh. (b) Comparison of the conformation of His255. The SRX RS^{CL} and SRX RS and SFX RS structures are shown by orange, yellow, hot pink, respectively. The sigma-A-weighted $2F_o$-F_c map (2.0 σ) is shown as a gray mesh. (c) Shift of the ligand chloride ion. The SRX RS^{CL} and SFX RS structures are shown by orange and hot pink, respectively. Chloride in the SRX RS^{CL} structure and that in the SFX RS structure is shown as a purple and green sphere, respectively.

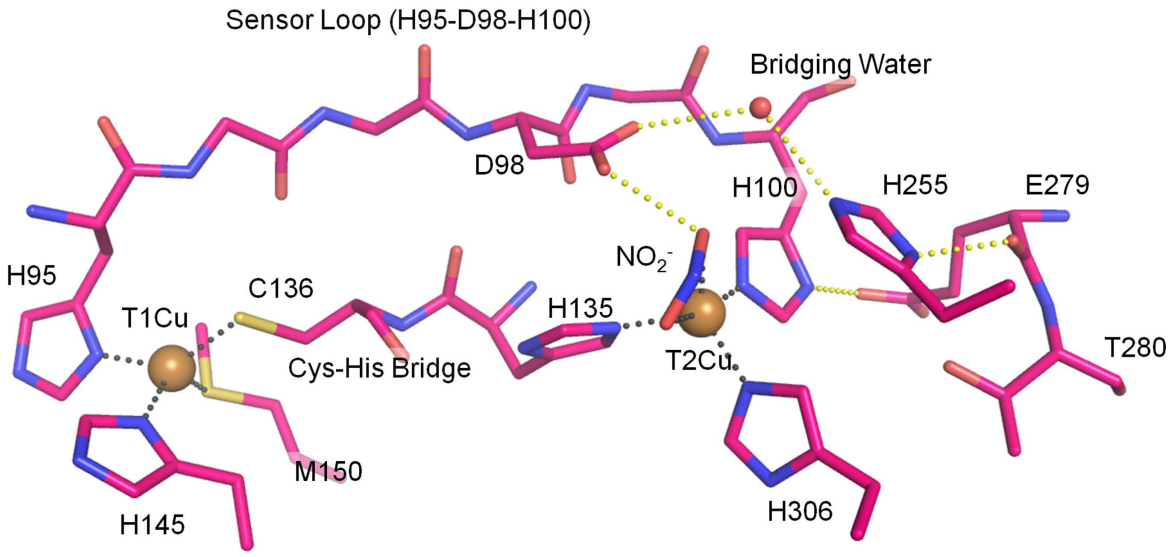

Fig. S15. Residues composing and connecting the T1Cu site and the T2Cu site. Dashed yellow and black lines show H-bonds and coordination bonds.

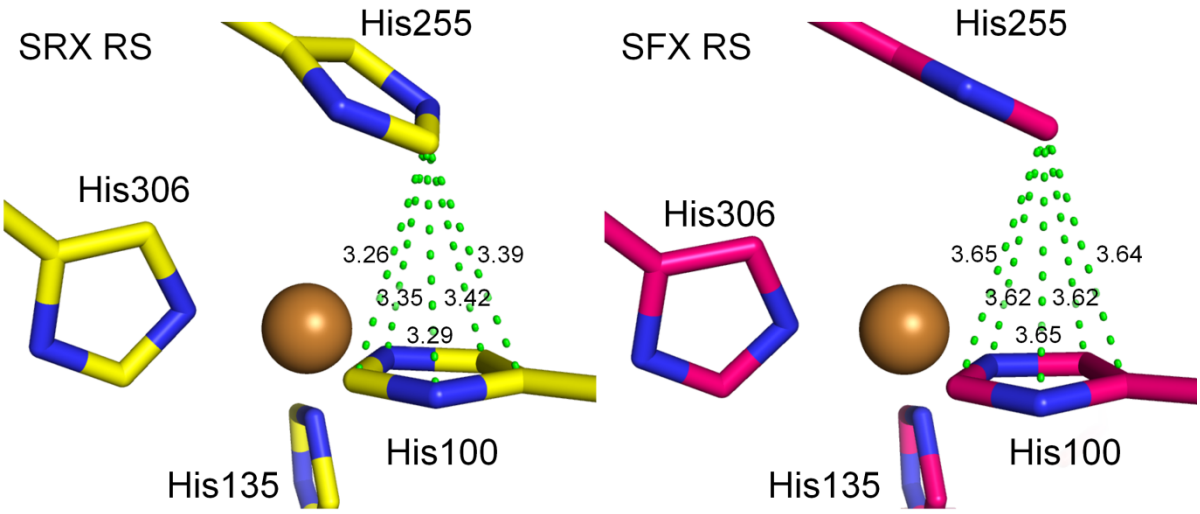

Fig. S16. Interaction between His255 and His100 (molecule A). Dashed green lines show the distance (Å) from the imidazole atoms of His100 to the $C^{\varepsilon 1}$ atom of His255.

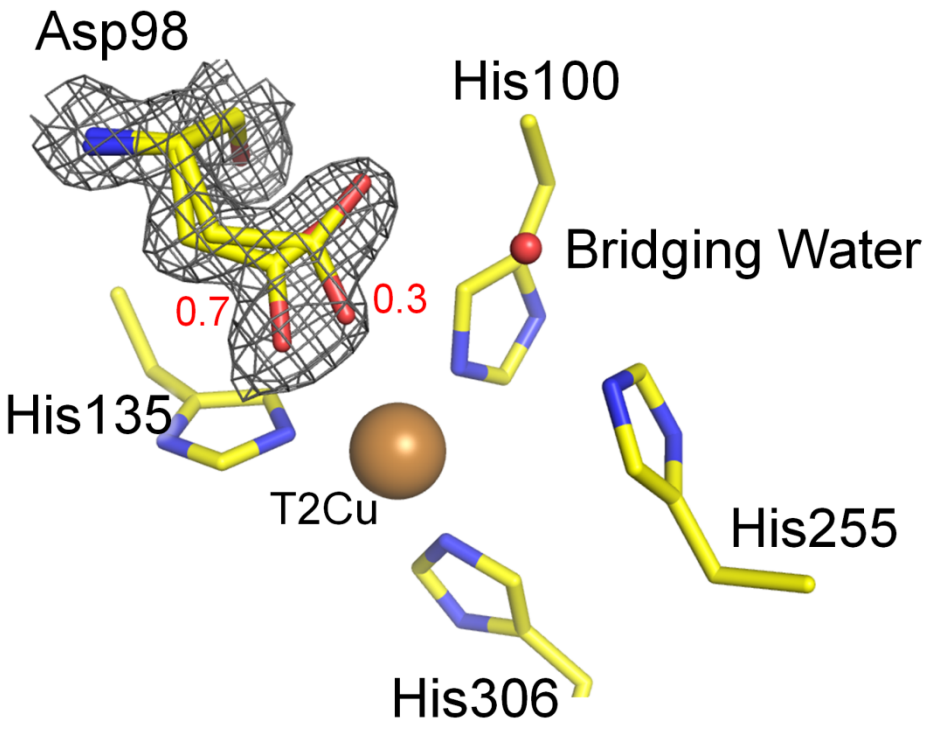

Fig. S17. Dual conformation of Asp98 in the SRX RS structure (molecule A). Values shown by red are the occupancies of each conformer. The sigma-A-weighted $2F_o–F_c$ map (1.2 σ) is shown as gray meshes.

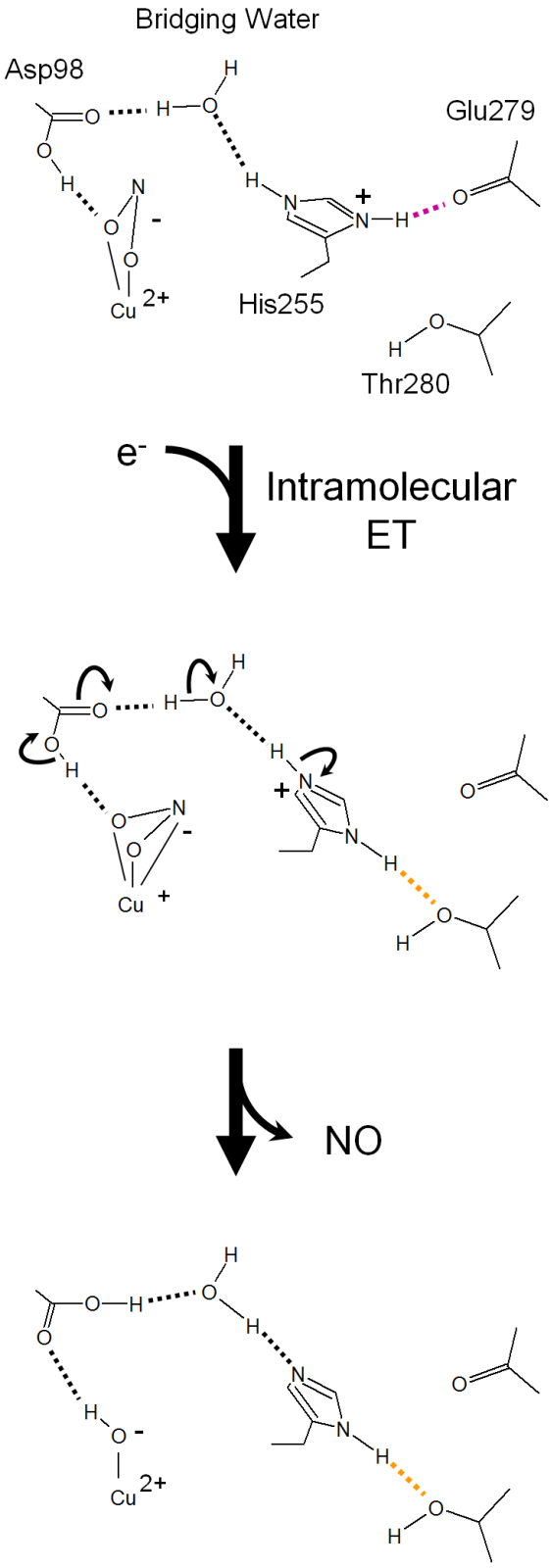

Fig. S18. The other possible reaction course predicted by computational chemistry (32). The rotation of His255 can trigger PT to NO_2^-.

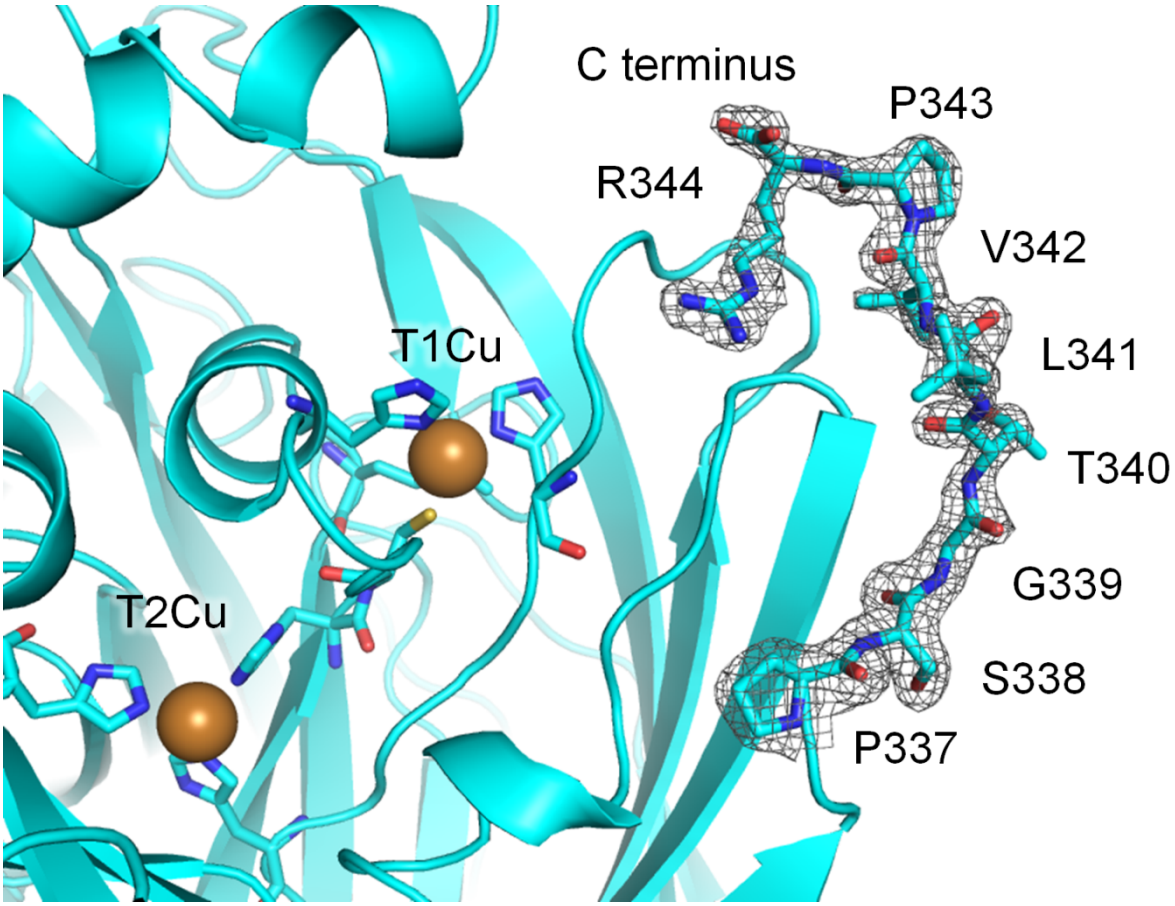

Fig. S19. The C-terminal residues of molecule B in the SFX NC structure. The sigma-A-weighted $2F_o–F_c$ (1.0 σ) map is shown as a gray mesh.

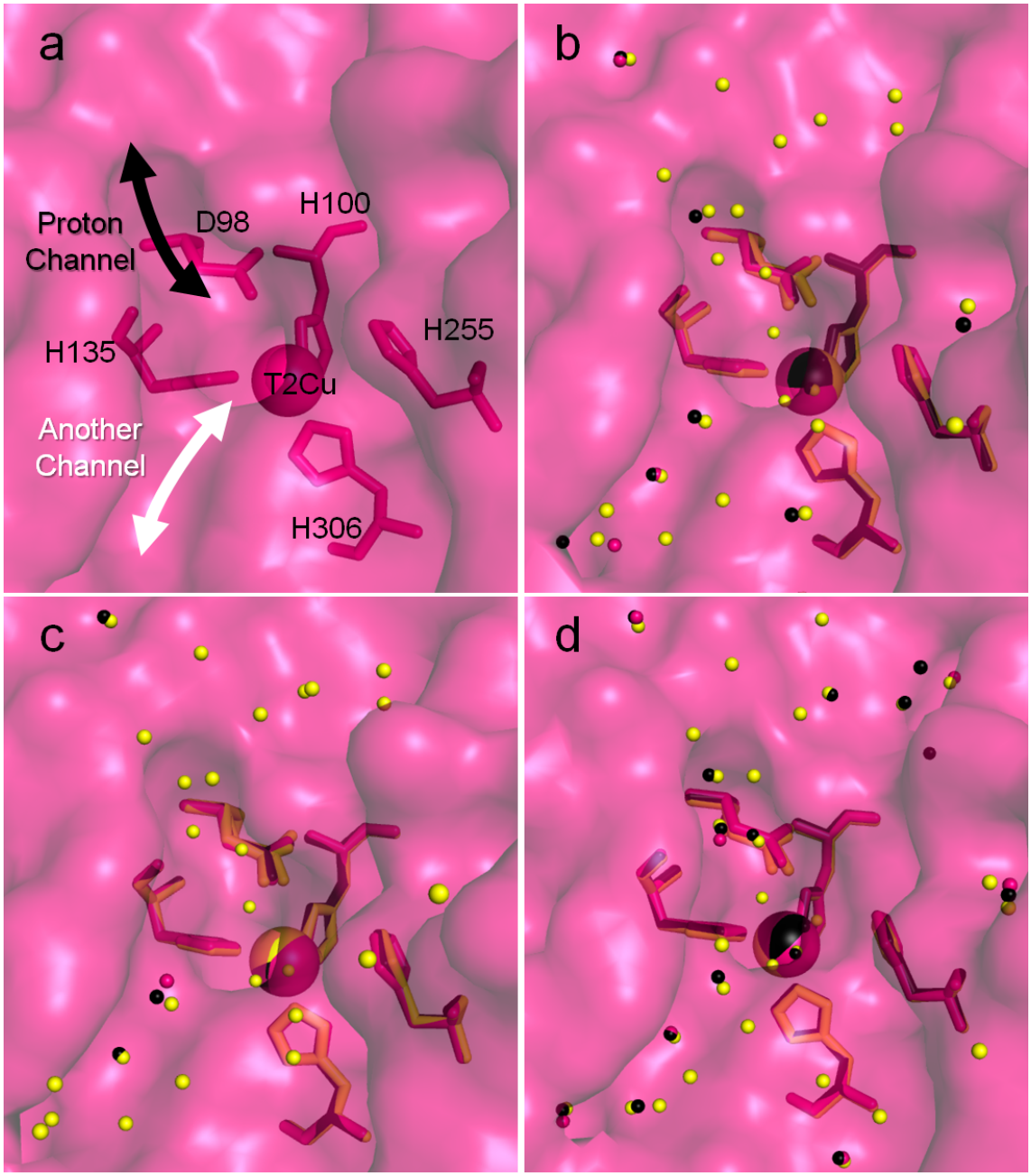

Fig. S20. Water molecules in the substrate pockets. (a) A putative proton substrate channel connecting the T2Cu site and the molecular surface (3, 4). (b), (c), and (d) describe the distribution of water molecules observed around each T2Cu site in an *Af*NiR trimer. Water molecules observed in the SRX RS, SRX RS^{RT}, and SFX RS structures are illustrated as small yellow, magenta, and black spheres, respectively.

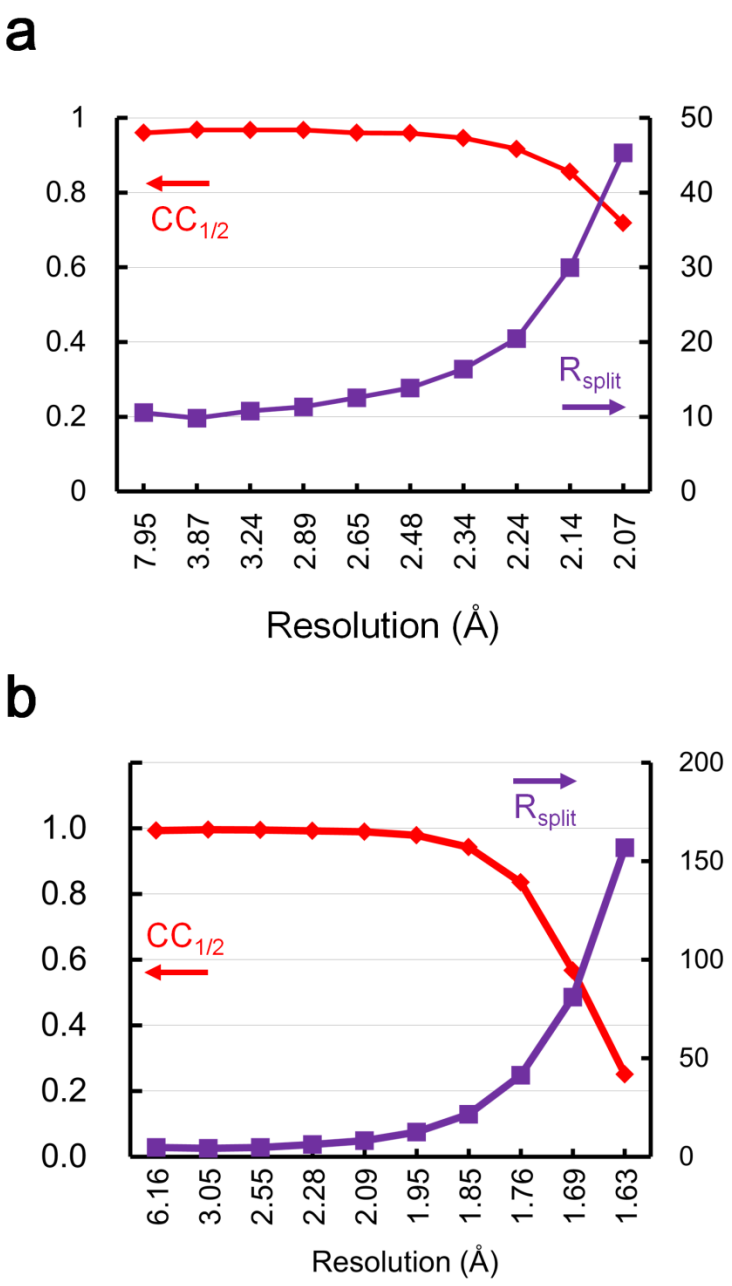

Fig. S21. $CC_{1/2}$ and R_{split} of the data of SFX RS (a) and the data of SFX NC (b).

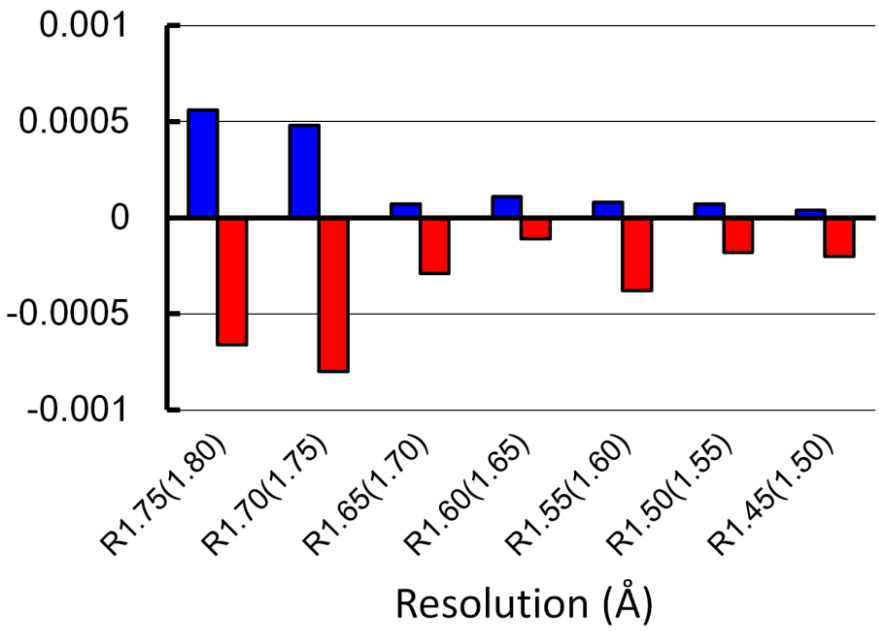

Fig. S22. Paired refinement for determination of resolution of the SFX NC structure. Rx (y) means that *R* values calculated at x Å resolution with the model refined at y Å resolution were compared with those using the model refined at x Å resolution. Blue and red columns show R_{work} and R_{free}, respectively.

4. SI Tables

Table S1 | Data collection and refinement statistics for the SRX RS structures

	SRX RS	SRX RS^{RT}
Data collection		
Beamline	SPring-8 BL26B1	SPring-8 BL26B2
X-ray dose (MGy)*	1.21	0.14
Temperature (K)	100	293
Wavelength (Å)	0.9500	0.9500
Space group	$P2_12_12_1$	$P2_12_12_1$
Unit cell *a*, *b*, *c* (Å)	61.9, 101.1, 146.2	62.8, 103.5, 147.2
Resolution range (Å)	50.0–1.20 (1.24–1.20)	50.0–1.56 (1.62–1.56)
R_{merge} (%)	7.30 (76.3)	7.10 (72.6)
$R_{p.i.m.}$ (%)	3.0 (33.5)	3.6 (37.5)
Completeness (%)	98.2 (96.6)	99.6 (96.1)
Unique reflections	281,187 (27,375)	136,155 (13,020)
$\langle I/\sigma(I)\rangle$	22.9 (2.2)	24.2 (2.2)
$CC_{1/2}$	(0.831)	(0.745)
Redundancy	6.4 (5.8)	4.9 (4.4)
Refinement		
Resolution (Å)	49.7–1.20 (1.23–1.20)	48.8–1.56 (1.60–1.56)
R_{work} (%)/ R_{free} (%)	12.9/16.8	14.9/17.7
No. of protein atoms	8,217	7,789
No. of ligand atoms and ions	86	6
No. of water molecules	1,094	453
Average *B* (Å^2)		
All	17.8	25.9
Protein atoms	16.4	25.5
Water atoms	27.4	32.7
Other atoms	30.8	19.0
Ramachandran plot (%)		
Favored	99.5	99.21
Allowed	0.5	0.79
Outliers	0	0
PDB code	4YSE	5F7B

* Average dose (exposed region) for a crystal was estimated with *RADDOSE-3D* (33).

Table S2 | Data collection and refinement statistics for the SFX RS structure

Data collection	
XFEL beamline	SACLA BL3 (EH4)
X-ray dose (MGy)	1.8–9.1
Temperature (K)	293 K
Wavelength (Å)	1.771
Space group	$P2_12_12_1$
Unit cell ***a*** **,*b*, *c* (Å)**	63.1, 103.8, 147.8
Resolution range (Å)	73.9–2.03
R_{split} **(%)**	11.24 (45.34)
Completeness (%)	100 (100)
Unique reflections	59,560 (5,853)
<*I*/σ (*I*)>	6.97 (2.17)
$CC_{1/2}$	0.980 (0.472)
Redundancy	147 (57.6)
Refinement	
Resolution range (Å)	73.9–2.03 (2.08–2.03)
R_{work} **(%)/** R_{free} **(%)**	16.4/20.3
No. of protein atoms	7,676
No. of heterogen atoms	9
No. of water molecules	246
Average *B* (Å^2)	
All	36.9
Protein atoms	36.8
Water atoms	38.3
Other atoms	34.9
Ramachandran plot (%)	
Favored	98.5
Allowed	1.5
Outliers	0
PDB code	4YSC

Table S3 | Geometries at the Cu sites in the RS structures (Molecule A, B, C)

parameter	SRX RS	SRX RS^{RT}	SFX RS
	I. Type 1 Cu-Ligand Distances (Å)		
T1Cu-H95N$^{\delta 1}$	2.06, 2.02, 2.06	2.05, 2.02, 1.98	2.22, 2.10, 2.03
T1Cu-C136S$^{\gamma}$	2.21, 2.23, 2.20	2.12, 2.19, 2.15	2.18, 2.13, 2.20
T1Cu-H145N$^{\delta 1}$	2.03, 1.98, 1.99	1.98, 1.99, 2.03	2.00, 2.02, 2.00
T1Cu-M150S$^{\delta}$	2.49, 2.50, 2.46	2.53, 2.55, 2.53	2.52, 2.63, 2.53
	II. Type 2 Cu-Ligand Distances (Å)		
T2Cu-H100N$^{\varepsilon 2}$	1.97, 2.00, 2.02	1.93, 2.03, 2.01	2.06, 2.11, 1.98
T2Cu-H135N$^{\varepsilon 2}$	2.01, 2.02, 1.98	2.05, 2.05, 2.00	2.14, 2.17, 2.04
T2Cu-H306N$^{\varepsilon 2}$	2.03, 1.99, 2.02	2.00, 2.02, 2.01	2.00, 2.04, 2.02
T2Cu-Wat0	2.32, 2.33, 2.32	2.20, 2.18, 2.28 [a)]	n/a
T2Cu-Wat0’	2.28, 2.34, 2.24	2.15, 1.99, 1.96 [b)]	n/a
T2Cu-Cl	n/a	n/a	2.21, 2.22, 2.22

a) Distances between T2Cu and water with 70% occupancy

b) Distances between T2Cu and water with 30% occupancy

Table S4 | Data collection and refinement statistics for the SRX NC structures

	SRX NC	SRX NC^{RT}
Data collection		
Beamline	SPring-8 BL26B1	SPring-8 BL26B2
X-ray dose (MGy)	0.95	0.21
Temperature (K)	100	293
Wavelength (Å)	0.9500	0.9500
Space group	$P2_12_12_1$	$P2_12_12_1$
Unit cell *a*, *b*, *c* (Å)	61.4, 102.2, 145.8	62.9, 103.7, 147.0
Resolution range (Å)	50.0–1.30 (1.35–1.30)	50.0–1.54 (1.60–1.54)
R_{merge} (%)	7.0 (91.5)	9.2 (> 100)
$R_{p.i.m.}$ (%)	2.3 (31.4)	4.0 (48.2)
Completeness (%)	99.9 (100)	100 (100)
Unique reflections	224,672 (2,236)	142,491 (14,098)
$\langle I/\sigma(I)\rangle$	32.6 (2.9)	23.2 (1.8)
$CC_{1/2}$	(0.846)	(0.683)
Redundancy	9.8 (9.4)	7.0 (7.0)
Refinement		
Resolution (Å)	49.5–1.30 (1.33–1.30)	48.9–1.54 (1.58–1.54)
R_{work} (%)/ R_{free} (%)	12.3/16.5	15.1/18.0
No. of protein atoms	7,933	7,789
No. of ligand atoms and ions	173	15
No. of water molecules	901	432
Average *B* (Å^2)		
All	18.8	24.9
Protein atoms	17.4	24.5
Water atoms	29.0	31.7
Other atoms	28.4	22.8
Ramachandran plot (%)		
Favored	99.22	99.01
Allowed	0.78	0.89
Outliers	0	0.1 (Gly229 Chain A)
PDB code	5D4H	5F7A

Table S5 | Geometries at the Cu sites in the NC structures (Molecule A, B, C)

parameter	SRX NC	SRX NC^{RT}	SFX NC
	I. Type 1 Cu-Ligand Distances (Å)		
T1Cu-H95N$^{\delta1}$	2.05, 2.02, 2.03	2.02, 2.01, 2.00	2.04, 2.00, 1.98
T1Cu-C136S$^{\gamma}$	2.20, 2.21, 2.19	2.13, 2.19, 2.16	2.21, 2.15, 2.16
T1Cu-H145N$^{\delta1}$	2.07, 2.04, 1.98	1.92, 1.93, 1.98	1.91, 2.01, 1.96
T1Cu-M150S$^{\delta}$	2.46, 2.49, 2.47	2.53, 2.60, 2.54	2.56, 2.58, 2.53
	II. Type 2 Cu-Ligand Distances (Å)		
T2Cu-H100N$^{\varepsilon2}$	2.02, 1.98, 2.02	1.97, 2.00, 1.98	2.00, 2.03, 1.98
T2Cu-H135N$^{\varepsilon2}$	2.02, 2.04, 2.02	2.05, 2.07, 2.03	2.06, 2.13, 2.05
T2Cu-H306N$^{\varepsilon2}$	2.04, 2.03, 2.02	2.03, 2.00, 2.03	1.98, 2.00, 2.00
T2Cu-ligand Wat	n/a, 2.14, 2.15	n/a	n/a
T2Cu-N$_{nitrite}$	2.10, 2.17, 2.21	2.24, 2.31, 2.27	2.27, 2.27, 2.30
T2Cu-O1$_{nitrite}$	2.16, 2.21, 2.18	2.09, 2.01, 2.09	2.14, 2.18, 2.09
T2Cu-O2$_{nitrite}$	2.01, 2.09, 2.11	2.15, 2.10, 2.12	1.93, 2.02, 2.06
	III. Other Distances (Å) and angles (°)		
D98O$^{\delta2}$-O2$_{nitrite}$	2.44, 2.44, 2.35	2.65, 2.73, 2.68	2.67, 2.70, 2.56
O1-N-O2 angle	117.8, 117.1, 115.5	116.1, 116.8, 114.4	125.1, 123.5, 123.3
Inclination of nitrite*	69.2, 70.4, 66.5	55.0, 33.1, 50.4	9.48, 39.1, 22.6

* Inclination of nitrite is the angle formed by the Cu-O1-O2 plane and the O1-N-O2 plane.

Table S6 | Geometries of nitrite in high resolution CuNiR structures (Å)

PDB code	1SJM[a] (ref. 27)	2BWI (ref. 4)	1KBV[b] (ref. 28)	3X1N (ref. 5)	1AS6[c] (ref. 29)
Resolution	1.40	1.10	1.95	1.55	1.80
T2Cu-$N_{nitrite}$	2.33 (2.31-2.36)[d]	2.15	2.33 (2.30-2.43)	2.21	2.43 (2.35-2.49)
T2Cu-$O1_{nitrite}$	2.32 (2.29-2.38)	2.19	2.57 (2.44-2.68)	2.52	2.28 (2.18-2.40)
T2Cu-$O2_{nitrite}$	2.06 (2.04-2.08)	1.98	2.03 (1.89-2.09)	2.13	2.20 (2.15-2.29)
Inclination of nitrite[e]	63.6 (58.8-68.7)	67.4	59.9 (34.7-74.1)	81.1	33.8 (6.22-64.62)

[a] Average of parameters of three monomers in the asymmetric unit. [b] Average of parameters of six monomers in the asymmetric unit. [c] Average of parameters of three monomers in the asymmetric unit. [d] Values in parentheses are minimum and maximum values. [e] Inclination of nitrite is the angle (degree) formed by the Cu-O1-O2 plane and the O1-N-O2 plane.

Table S7 | Data collection and refinement statistics for the SFX NC structure

Data collection	
XFEL beamline	SACLA BL3 (EH4)
X-ray dose (MGy)	5.5–27.3
Temperature (K)	293 K
Wavelength (Å)	1.149
Space group	$P2_12_12_1$
Unit cell ***a*** **,*b*, *c* (Å)**	63.0, 103.0, 147.4
Resolution range (Å)	28.97–1.60 (1.66–1.60)
R_{split} **(%)**	5.01 (156.79)
Completeness (%)	100 (100)
Unique reflections	120,357 (11,892)
<*I*/σ (*I*)>	11.87 (1.00)
$CC_{1/2}$	0.996 (0.251)
CC_{ano}	0.0289 (-0.00109)
Redundancy	1079.0 (1021.6)
Refinement	
Resolution range (Å)	28.97–1.60 (1.63–1.60)
R_{work} **(%)/** R_{free} **(%)**	16.5/19.6
No. of protein atoms	7,915
No. of heterogen atoms	15
No. of water molecules	330
Average ***B*** **(Å^2)**	
All	37.0
Protein atoms	36.9
Water atoms	38.7
Other atoms	36.5
Ramachandran plot (%)	
Favored	98.7
Allowed	1.3
Outliers	0
PDB code	5D4I

Table S8 | Data collection and refinement statistics for the SRX RS^{CL} structure

Data collection	
Synchrotron beamline	SPring-8 BL44XU
X-ray dose (MGy)	0.08
Temperature (K)	100
Wavelength (Å)	1.7500
Space group	$P2_12_12_1$
Unit cell *a*, *b*, *c* (Å)	61.4, 102.2, 144.5
Resolution range (Å)	50.0–2.00 (2.07–2.00)
R_{merge} (%)	15.0 (> 100)
$R_{p.i.m.}$ (%)	3.9 (39.5)
Completeness (%)	100 (100)
Unique reflections	62,159 (6,125)
$\langle I/\sigma(I)\rangle$	19.2 (1.80)
$CC_{1/2}$	(0.769)
Redundancy	24.2 (24.0)
Refinement	
Resolution (Å)	24.8–2.00 (2.05–2.00)
R_{work} (%)/ R_{free} (%)	18.2/23.2
No. of protein atoms	7,683
No. of ligand atoms and ions	81
No. of water molecules	385
Average *B* (Å^2)	
All	33.1
Protein atoms	32.8
Water atoms	36.2
Other atoms	46.7
Ramachandran plot (%) (Å^2)	
Favored	98.2
Allowed	1.8
Outliers	0
PDB code	5D4J

Table S9 | Geometries at the Cu sites in the SRX RS^{CL} structure (Molecule A, B, C)

parameter	SRX RS^{CL}
	I. Type 1 Cu-Ligand Distances (Å)
T1Cu-H95N$^{\delta 1}$	2.33, 2.12, 1.98
T1Cu-C136S$^{\gamma}$	2.12, 2.13, 2.28
T1Cu-H145N$^{\delta 1}$	1.98, 2.05, 2.08
T1Cu-M150S$^{\delta}$	2.44, 2.43, 2.53
	II. Type 2 Cu-Ligand Distances (Å)
T2Cu-H100N$^{\varepsilon 2}$	2.10, 1.99, 2.04
T2Cu-H135N$^{\varepsilon 2}$	2.06, 2.12, 2.11
T2Cu-H306N$^{\varepsilon 2}$	2.05, 2.09, 2.06
T2Cu-Cl	2.27, 2.34, 2.17

Table S10 | Observed residues in the present structures.

	SRX RS	**SRX RS^{RT}**	**SRX RS^{CL}**	**SRX NC**	**SRX NC^{RT}**	**SFX RS**	**SFX NC**
Resolution (Å)	1.20	1.56	2.00	1.30	1.54	2.03	1.60
Beamline	BL26B1	BL26B2	BL44XU	BL26B1	BL26B2	BL3	BL3
Molecule A	A4 – T340	A4 – G339	A6 – T340	A4 – T340	A4 – G339	A4 – G339	A6 – G339
Molecule B	A4 – T340	A4 – T340	A4 – G339	A4 – R344	A4 – T340	A4 – G339	A4 – R344
Molecule C	A4 – T340	A4 – G339	A4 – G339	A4 – V342	A4 – G339	A4 – S338	A6 – G339
Total amino acids	1011 aa	1009 aa	1007 aa	1017 aa	1009 aa	1007 aa	1009 aa

5. SI References

(1) Nishiyama M, *et al.* (1993) Cloning and characterization of a nitrite reductase gene from *Alcaligenes faecalis* and its expression in *Escherichia coli*. *J Gen Microb* 139:725-733.

(2) Hough MA, Antonyuk SV, Strange RW, Eady RR, & Hasnain SS (2008) Crystallography with online optical and X-ray absorption spectroscopies demonstrates an ordered mechanism in copper nitrite reductase. *J Mol Biol* 378(2):353-361.

(3) Leferink NG, *et al.* (2011) Proton-coupled electron transfer in the catalytic cycle of *Alcaligenes xylosoxidans* copper-dependent nitrite reductase. *Biochemistry* 50(19):4121-4131.

(4) Antonyuk SV, Strange RW, Sawers G, Eady RR, & Hasnain SS (2005) Atomic resolution structures of resting-state, substrate- and product-complexed Cu-nitrite reductase provide insight into catalytic mechanism. *Proc Natl Acad Sci USA*102(34):12041-12046.

(5) Fukuda Y & Inoue T (2015) High-temperature and high-resolution crystallography of thermostable copper nitrite reductase. *Chem Commun* 51(30):6532-6535.

(6) Lawton TJ, Bowen KE, Sayavedra-Soto LA, Arp DJ, & Rosenzweig AC (2013) Characterization of a nitrite reductase involved in nitrifier denitrification. *J Biol Chem* 288(35):25575-25583.

(7) MacPherson IS, Rosell F, Scofield M, Mauk AG, & Murphy MEP (2010) Directed evolution of copper nitrite reductase to a chromogenic reductant. *Protein Eng Des Sel* 23(3):137-145.

(8) Wijma HJ, Jeuken LJ, Verbeet MP, Armstrong FA, & Canters GW (2006) A random-sequential mechanism for nitrite binding and active site reduction in copper-containing nitrite reductase. *J Biol Chem* 281(24):16340-16346.

(9) Ueno G, *et al.* (2006) RIKEN structural genomics beamlines at the SPring-8; high throughput protein crystallography with automated beamline operation. *J Struct Funct Genomics* 7(1):15-22.

(10) Sugahara M, *et al*. (2014) Grease matrix as a versatile carrier of proteins for serial crystallography. *Nat Methods* 12(1):61-63.

(11) Tono T, *et al*. (2015) Diverse application platform for hard X-ray diffraction in SACLA (DAPHNIS): application to serial protein crystallography using an X-ray free-electron laser. *J Synch Rad* 22:532-537.

(12) Kameshima T, *et al.* (2014) Development of an X-ray pixel detector with

multi-port charge-coupled device for X-ray free-electron laser experiments. *Rev Sci Instrum* 85:033110.

(13) Yumoto H, *et al.* (2012) Focusing of X-ray free-electron laser pulses with reflective optics. *Nat Photonics* 7:43-47.

(14) Son SK, Chapman HN, & Santra R (2011) Multiwavelength anomalous diffraction at high x-ray intensity. *Phys Rev Lett* 107(21):218102.

(15) Nass K, *et al.* (2015) Indications of radiation damage in ferredoxin microcrystals using high-intensity X-FEL beams. *J Synch Rad* 22:225-238.

(16) White TA *et al.* (2013) Crystallographic data processing for free-electron laser sources. *Acta Cryst D* 69:1231-1240.

(17) Joti Y, *et al.* (2015) Data acquisition system for X-ray free-electron laser experiments at SACLA. *J Synch Rad* 22:571-576.

(18) Fukuda Y, *et al*. (2014) Structural insights into the function of a thermostable copper-containing nitrite reductase. *J Biochem* 155(2):123-135.

(19) Nakane T, *et al*. (2015) Native sulfur/chlorine SAD phasing for serial femtosecond crystallography. *Acta Cryst D* 71:2519–2525.

(20) Kabsch W (2010) XDS. *Acta Cryst D* 66:125-132.

(21) Hendrickson WA & Teeter MM (1981) Structure of the hydrophobic protein crambin determined directly from the anomalous scattering of sulphur. *Nature* 290:107–113.

(22) Karplus PA & Diederichs K (2012) Linking crystallographic model and data quality. *Science* 336(6084):1030-1033.

(23) Evans PR & Murshudov GN (2013) How good are my data and what is the resolution? *Acta Cryst D* 69:1204-1214.

(24) Bublitz M, *et al.*(2015) Structural studies of P-type ATPase–ligand complexes using an X-ray free-electron laser. *IUCrJ* 2:409-420.

(25) Larkin MA, *et al*. (2007) Clustal W and Clustal X version 2.0. *Bioinformatics* 23(21):2947-2948.

(26) Robert X & Gouet P (2014) Deciphering key features in protein structures with the new ENDscript server. *Nucl. Acids Res*. 42(W1):W320-W324.

(27) Tocheva EI, Rosell FI, Mauk AG, & Murphy ME (2004) Side-on copper-nitrosyl coordination by nitrite reductase. *Science* 304(5672):867-870.

(28) Boulanger MJ & Murphy MEP (2002) Crystal structure of the soluble domain of the major anaerobically induced outer membrane protein (AniA) from pathogenic *Neisseria*: a new class of copper-containing nitrite reductases. *J Mol Biol* 315: 1111-1127.

(29) Murphy MEP, Turley S, & Adman ET (1997) Structure of nitrite bound to

copper-containing nitrite reductase from *Alcaligenes faecalis*. *J Biol Chem* 272(45):28455-28460.

(30) Jacobson F*, et al.* (2005) Structures of the oxidized and reduced forms of nitrite reductase from *Rhodobacter sphaeroides* 2.4.3 at high pH: changes in the interactions of the type 2 copper. *Acta Cryst D* 61(Pt 9):1190-1198.

(31) Jacobson F*, et al.* (2007) pH dependence of copper geometry, reduction potential, and nitrite affinity in nitrite reductase. *J Biol Chem* 282(9):6347-6355.

(32) Ghosh S, Dey A, Sun Y, Scholes CP, & Solomon EI (2009) Spectroscopic and computational studies of nitrite reductase: proton induced electron transfer and backbonding contributions to reactivity. *J Am Chem Soc* 131:277-288.

(33) Zeldin OB, Gerstel M, & Garman EF (2013) *RADDOSE-3D*: time- and space-resolved modelling of dose in macromolecular crystallography. *J Appl Cryst* 46:1225-1230.